Coenzyme A fuels T cell anti-tumor immunity

St. Paul, Michael; Saibil, Samuel D.; Han, SeongJun; Israni-Winger, Kavita; Lien, Scott C.; Laister, Rob C.; Sayad, Azin; Penny, Susanne; Amaria, Rodabe N.; Haydu, Lauren E.; Garcia-Batres, Carlos R.; Mulder, David T.; Robert-Tissot, Céline; Gold, Matthew J.; Tran, Charles W.; Elford, Alisha R.; Nguyen, Linh T.; Pugh, Trevor J.; Pinto, Devanand M.; Wargo, Jennifer A.; Ohashi, Pamela S.

Publisher's version / Version de l'éditeur:
https://doi.org/10.1016/j.cmet.2021.11.010
Cell Metabolism, 33, 12, pp. 2415-2427.e6, 2021-12-07

Article

Cell Metabolism

Coenzyme A fuels T cell anti-tumor immunity

Graphical abstract

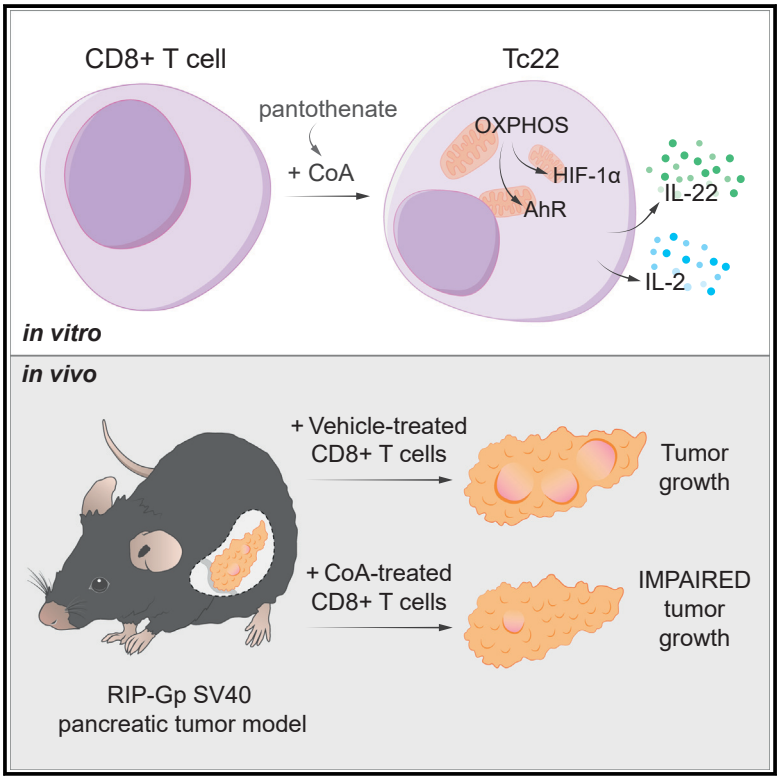

Highlights

- CD8$^+$ Tc22 cells are metabolically distinct and rely on OXPHOS for polarization
- CoA induces Tc22 and OXPHOS in the absence of polarizing cytokines via HIF-1α and AhR
- CoA-treated T cells demonstrate enhanced anti-tumor function and persistence
- The CoA precursor pantothenate enhances response to anti-PDL1 therapy *in vivo*

Authors

Michael St. Paul, Samuel D. Saibil, SeongJun Han, ..., Devanand M. Pinto, Jennifer A. Wargo, Pamela S. Ohashi

Correspondence

pohashi@uhnresearch.ca

In brief

St. Paul et al. demonstrate that activating CD8$^+$ T cells in the presence of coenzyme A (CoA) induced Tc22 polarization and OXPHOS in the absence of polarizing cytokines via activation of HIF-1α and AhR transcription factors. Targeting the pantothenate/CoA pathway enhanced anti-tumor responses, revealing an unappreciated role for pantothenate metabolism in enhancing T cell anti-tumor function.

St. Paul et al., 2021, Cell Metabolism *33*, 2415–2427
December 7, 2021
https://doi.org/10.1016/j.cmet.2021.11.010

CellPress

Cell Metabolism

CellPress

Article

Coenzyme A fuels T cell anti-tumor immunity

Michael St. Paul,[1,2,6] Samuel D. Saibil,[1,2,6] SeongJun Han,[1,2] Kavita Israni-Winger,[1,2] Scott C. Lien,[1,2] Rob C. Laister,[1] Azin Sayad,[1] Susanne Penny,[3] Rodabe N. Amaria,[4] Lauren E. Haydu,[5] Carlos R. Garcia-Batres,[1] Meghan Kates,[1,2] David T. Mulder,[1] Céline Robert-Tissot,[1] Matthew J. Gold,[1] Charles W. Tran,[1,2] Alisha R. Elford,[1] Linh T. Nguyen,[1] Trevor J. Pugh,[1] Devanand M. Pinto,[3] Jennifer A. Wargo,[5] and Pamela S. Ohashi[1,2,7,*]

[1]Princess Margaret Cancer Centre, University Health Network, Toronto, ON M5G 2C1, Canada
[2]Department of Immunology, University of Toronto, Toronto, ON M5S 1C1, Canada
[3]National Research Council, Human Health Therapeutics, Halifax, NS B3H 3Z1, Canada
[4]Department of Melanoma Medical Oncology, MD Anderson Cancer Center, Houston, TX 77030, USA
[5]Department of Surgical Oncology, MD Anderson Cancer Center, Houston, TX 77030, USA
[6]These authors contributed equally
[7]Lead contact
*Correspondence: pohashi@uhnresearch.ca
https://doi.org/10.1016/j.cmet.2021.11.010

SUMMARY

Metabolic programming is intricately linked to the anti-tumor properties of T cells. To study the metabolic pathways associated with increased anti-tumor T cell function, we utilized a metabolomics approach to characterize three different CD8$^+$ T cell subsets with varying degrees of anti-tumor activity in murine models, of which IL-22-producing Tc22 cells displayed the most robust anti-tumor activity. Tc22s demonstrated upregulation of the pantothenate/coenzyme A (CoA) pathway and a requirement for oxidative phosphorylation (OXPHOS) for differentiation. Exogenous administration of CoA reprogrammed T cells to increase OXPHOS and adopt the CD8$^+$ Tc22 phenotype independent of polarizing conditions via the transcription factors HIF-1α and the aryl hydrocarbon receptor (AhR). In murine tumor models, treatment of mice with the CoA precursor pantothenate enhanced the efficacy of anti-PDL1 antibody therapy. In patients with melanoma, pre-treatment plasma pantothenic acid levels were positively correlated with the response to anti-PD1 therapy. Collectively, our data demonstrate that pantothenate and its metabolite CoA drive T cell polarization, bioenergetics, and anti-tumor immunity.

INTRODUCTION

Immunotherapy has revolutionized the treatment of cancer. Current treatment modalities range from cell therapy using tumor-specific T cells, including those that express transgenic T cell receptors (TCRs) and chimeric antigen receptors (CARs), to antibodies targeting important immunological checkpoint molecules, such as PD1 (Waldman et al., 2020). Despite their success, however, many patients fail to respond to immunotherapy. The identification of novel methods to enhance the efficacy of immunotherapeutic modalities is an area of active investigation. Recently, manipulating the metabolic programming of anti-tumor T cells to enhance cellular bioenergetics has emerged as a promising means to enhance the anti-tumor activity of T cells, both in the context of cellular therapies and immune checkpoint inhibitors (Buck et al., 2016; Chamoto et al., 2017; Saibil et al., 2019; Scharping et al., 2016; Zhang et al., 2017).

Metabolic processes influence many aspects of T cell function including their activation, differentiation, and effector function (Gerriets et al., 2015; Johnson et al., 2018; O'Neill et al., 2016; Pearce et al., 2013). In the context of immunotherapy, it is becoming increasingly clear that enhanced mitochondrial metabolism and oxidative phosphorylation (OXPHOS) in T cells are associated with increased persistence and effector activity resulting in robust anti-tumor responses (Chang and Pearce, 2016). This enhanced OXPHOS can be achieved by *ex vivo* manipulation of T cells such as by enhancing fatty acid oxidation (FAO) (Saibil et al., 2019) or by increasing mitochondrial biogenesis (Scharping et al., 2016) and mitochondrial fusion (Buck et al., 2016). Moreover, targeting T cell co-stimulatory molecules such as 4-1BB can improve oxidative metabolism and anti-tumor activity (Menk et al., 2018). These findings were echoed in CAR T cells, as it was shown that CARs with a 4-1BB signaling domain demonstrated increased persistence and bioenergetics compared to those with a CD28 domain (Kawalekar et al., 2016). In addition to enhancing cellular therapy, the *in vivo* modulation of T cell oxidative metabolism has shown success in boosting responses to anti-PDL1 therapy in murine models (Chamoto et al., 2017; Zhang et al., 2017). Together, these findings indicate that targeting T cell metabolism can re-invigorate anti-tumor responses in the context of both cellular therapy and checkpoint blockade.

In the present paper, we sought to identify novel metabolic pathways in T cells that could be targeted to enhance bioenergetics and anti-tumor activity. Using a metabolomics approach, we characterized the metabolism of three different functional subsets of effector CD8$^+$ T cells, each shown to have different degrees of anti-tumor activity: the conventional IFN-γ-producing Tc1 cells, IL-17-producing Tc17 cells, and IL-22-producing Tc22

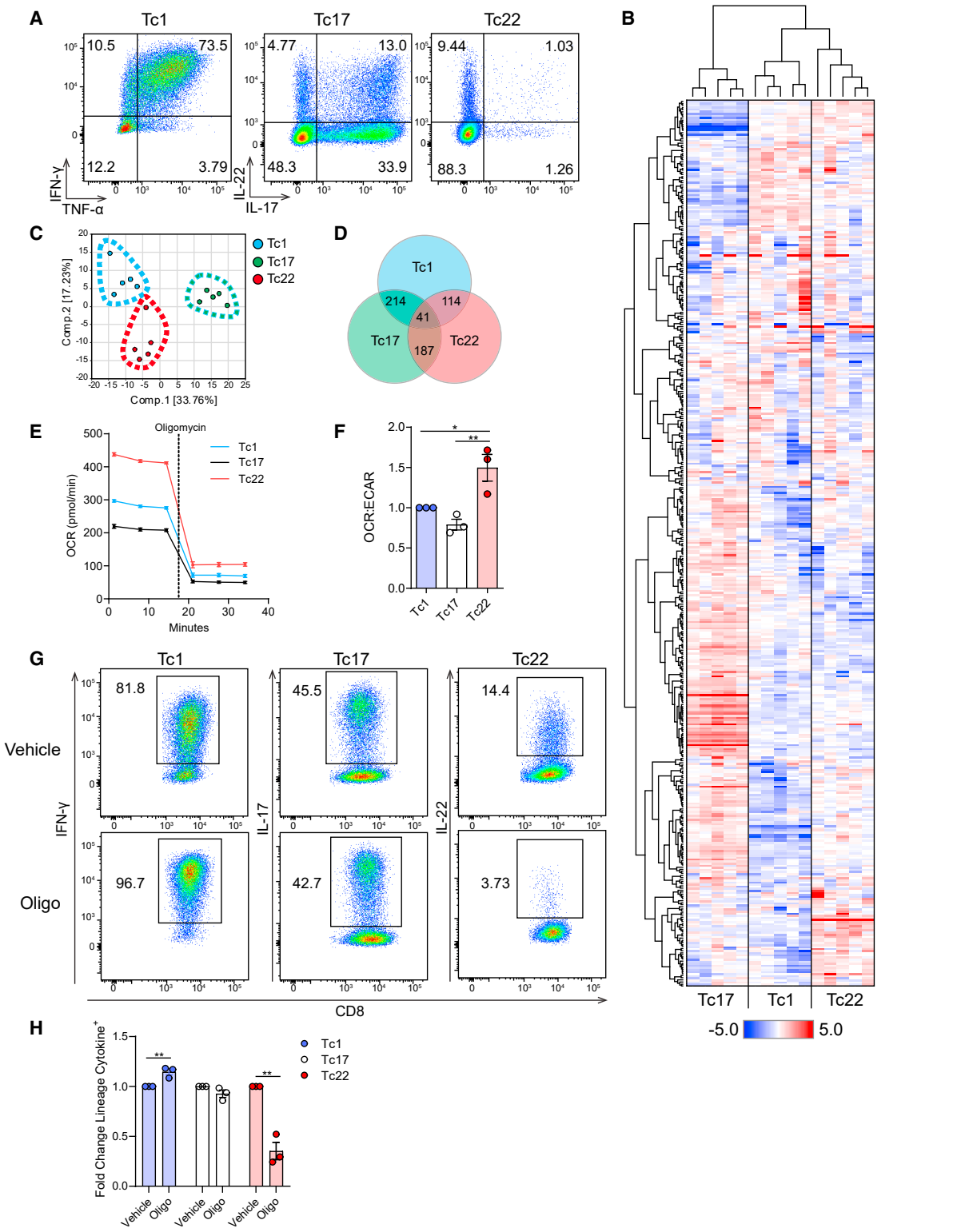

Figure 1. Tc22 polarization is dependent on oxidative phosphorylation

(A) Cytokine profile of CD8$^+$ T cells activated for 3 days in the presence of polarizing cytokines.

(B and C) Metabolites were extracted and quantified from polarized Tc subsets derived from 5 mice and displayed as a (B) heatmap or (C) PCA plot. Heatmap values represent relative abundance of metabolites.

(D) Number of significantly different metabolites relative to each subset.

(legend continued on next page)

cells (Mittrücker et al., 2014; St Paul and Ohashi, 2020; St Paul et al., 2020). We found the pantothenate/coenzyme A (CoA) metabolic pathways to be enriched in Tc22 cells and identified CoA as a reagent able to induce OXPHOS and Tc22 differentiation in the absence of polarizing cytokines. Moreover, treating T cells with CoA enhanced anti-tumor activity in multiple mouse models, and the *in vivo* administration of the CoA-precursor pantothenate enhanced anti-PDL1 therapy in pre-clinical models. Importantly, we correlated increased pre-treatment plasma pantothenic acid levels with response to anti-PD1 antibody therapy in a cohort of patients with advanced melanoma. These findings identify the pantothenate/CoA pathway as a promising target to enhance oxidative metabolism in T cells and to augment the efficacy of immunotherapy.

RESULTS

Tc22 polarization is dependent on oxidative phosphorylation

Multiple different subsets of effector $CD8^+$ T cells have been identified, each with distinct cytokine profiles, effector function, and anti-tumor properties (St Paul and Ohashi, 2020). Previously, we have found that a subset of $CD8^+$ T cells that produce IL-22, referred to as Tc22 cells, demonstrated robust anti-tumor properties relative to the IFN-γ-producing Tc1 and IL-17-producing Tc17 cell subsets (St Paul et al., 2020). Of note, Tc22 cells did not require IL-22 for their ability to control tumor growth, as blocking IL-22 did not result in impaired anti-tumor function (Figure S1). This suggests that other aspects of T cell function that occur in conjunction with Tc22 lineage polarization may be mediating this enhanced anti-tumor activity. Given that Tc22 cells were previously shown to have elevated levels of ATP and increased expression of components of the mitochondrial electron transport chain (St Paul et al., 2020), we hypothesized that Tc22 cells have a unique metabolic program that contributes to their anti-tumor activity, and that IL-22 production may occur as a consequence of this metabolic programming. Furthermore, we reasoned that elucidating these metabolic pathways unique to Tc22 cells could lead to novel therapeutic targets to metabolically reprogram $CD8^+$ T cells and potentially enhance immunotherapy. Accordingly, to identify metabolic programs associated with the Tc22 lineage, we set out to perform in-depth metabolic analysis on differentiated Tc1, Tc17, and Tc22 subsets that were generated by activating $CD8^+$ T cells in the presence of lineage-specific polarizing cytokines (Figure 1A).

The mitochondria are sites of cellular respiration and are essential for biochemical reactions comprising the tricarboxylic acid (TCA) cycle and OXPHOS. Given this, we first sought to characterize the mitochondrial phenotype and the uptake of nutrients that can fuel OXPHOS including glucose and fatty acids among the three Tc subsets. Despite the fact that each Tc subset underwent robust proliferation during polarization (Figures S2A and S2B), Tc17 cells displayed a decrease in mitochondrial mass, membrane potential, glucose uptake, and fatty acid uptake relative to Tc1 and Tc22 cells (Figures S2C–S2F). This suggests a decreased utilization of mitochondrial OXPHOS in Tc17 cells relative to other subsets and potentially different metabolic programming. To further elucidate these differences in the global metabolic profile of the Tc1, Tc17, and Tc22 subsets, we performed mass spectrometry employing an untargeted metabolomics approach (Figure 1B). Using principal component analysis (PCA) and unsupervised hierarchical cluster analysis, we found that each Tc subset formed a unique cluster (Figures 1B and 1C) with at least 100 metabolites significantly altered between each individual subset (Figure 1D). Some of the most notable differences in metabolites were in the levels of glycolytic and TCA cycle intermediates, despite having minimal alterations of these pathways at the transcriptional level (Figures S2G–S2K). To further investigate this, we analyzed the respective utilization of glycolysis versus OXPHOS of the three Tc subsets using the Seahorse Bioanalyzer. This method allows the concurrent measurement of the oxygen consumption rate (OCR—indicative of OXPHOS) and the extracellular acidification rate (ECAR—indicative of glycolysis) in real time (van der Windt et al., 2016). These studies confirmed that Tc17 cells did indeed display less utilization of OXPHOS. Interestingly, we also found that the Tc22 subset had the highest basal OCR (Figure 1E) and the highest ratio of OCR to ECAR among the three subsets (Figure 1F), similar to what has previously been reported for memory $CD8^+$ T cells relative to activated effector cells (van der Windt et al., 2012). Moreover, this enhanced OCR in Tc22 cells was coupled to ATP production as the addition of oligomycin, an inhibitor of ATP synthase and oxidative metabolism, led to a marked reduction in OCR (Figure 1E). These data were consistent with our previous data that Tc22 cells demonstrated increased levels of intracellular ATP (St Paul et al., 2020). Collectively, these data confirmed different metabolic programming among the different Tc subsets and suggest a link between oxidative metabolism and the Tc22 lineage.

To further explore this connection between OXPHOS and Tc22 cells, we investigated the requirement for IL-22 production to promote oxidative metabolism. We found that the increased OPXHOS in Tc22 cells occurred independently of IL-22 production, as comparable OCR levels were observed in wild-type (WT) and IL-22-deficient Tc22 cells (Figure S2L). Moreover, comparable OCR levels were observed following depletion of IL-22 producing cells from bulk cultures of T cells exposed to Tc22-inducing cytokines prior to seahorse analysis. These data indicate that exposure to Tc22-inducing cytokines induce an oxidative phenotype in the cells, even in those not found to be actively secreting IL-22 (Figure S2M). This is in accordance with previous analysis that showed that cells polarized to various lineages all expressed lineage defining markers irrespective of their ability to produce cytokines (St Paul et al., 2020). Together, these findings demonstrate that IL-22 production is not required to establish the oxidative metabolic phenotype of Tc22 cells.

(E) Oxygen consumption rate (OCR) before and after addition of oligomycin.
(F) Basal OCR:ECAR ratio pooled from multiple independent experiments and normalized to Tc1 cells (n = 3 ± SEM).
(G) Cytokine profile of $CD8^+$ Tc subsets polarized in the presence of oligomycin (Oligo) or vehicle control.
(H) Data from (G) pooled from multiple independent experiments and expressed as fold change compared to vehicle (n = 3 ± SEM).
Results shown are representative of at least 3 independent experiments (A, E, and G). Statistical significance was calculated using (F) ANOVA with Sidak post hoc test or (H) t test. *$p < 0.05$, **$p < 0.01$.

It remained unclear, however, whether IL-22 production is dependent on this metabolic shift toward oxidative metabolism and mitochondrial ATP generation in Tc22 cells. To address this possibility, we activated cells in Tc22 conditions in the presence of oligomycin, an inhibitor of oxidative metabolism, and noted a decrease in IL-22 production (Figures 1G and 1H). In contrast, oligomycin did not affect IL-17 production by Tc17 cells and enhanced IFN-γ production by cells polarized to the Tc1 lineage, which is consistent with published reports linking glycolytic metabolism to the production of IFN-γ (Chang et al., 2013) (Figures 1G and 1H). Collectively, these data establish that Tc22-inducing cytokines drive an oxidative metabolic program that is important for polarization to the Tc22 lineage.

Memory $CD8^+$ T cells have previously been shown to rely upon an oxidative metabolic program via FAO (van der Windt et al., 2012). Accordingly, we next investigated the possibility that Tc22s were memory-like cells given this shared utilization of OXPHOS. Surface marker analysis revealed that Tc22s resemble effector T cells, similar to both Tc1 and Tc17 cells (St Paul et al., 2020) (Figure S3A). Moreover, Tc22 cells also do not resemble T memory stem cells (Tscm) (Gattinoni et al., 2012), as Tc22 cells expressed similar levels of Tscm markers compared to other Tc subsets (Figure S3B). Furthermore, as FAO is key to memory cell function, we found that Tc22 cells did not upregulate genes associated with FAO and had similar levels of lipids as other Tc subsets (Figures S3C–S3F). Lastly, treatment with the carnitine palmitoyltransferase 1a (CPT1a) inhibitor etomoxir, an inhibitor of the rate-limiting step of FAO, had no effect on IL-22 production (Figure S3G). This finding suggested that Tc22 polarized cells do not depend on FAO to fuel OXPHOS, ATP, and subsequent IL-22 production. Together, this distinguishes the metabolic program of Tc22 cells from memory $CD8^+$ T cells and other oxidative T cell lineages, such as $CD4^+$ Tregs, which both rely on FAO for their differentiation and oxidative metabolic phenotype (Michalek et al., 2011; O'Sullivan et al., 2014; Pearce et al., 2009). These data also reinforce that Tc22 cells are an effector lineage, with little similarity to memory T cells or Tscm cells other than the utilization of mitochondrial oxidative metabolism. These data demonstrate that enhanced utilization of oxidative metabolism is a distinct metabolic phenotype of Tc22 cells among activated $CD8^+$ T cell effector subsets and that this metabolic phenotype is associated with polarization to this lineage.

Pantothenate/CoA pathway is enriched in Tc22 cells and augments IL-22 production

To further characterize this oxidative metabolic phenotype of Tc22s, we performed metabolic pathway analysis on the metabolomics data of the Tc subsets and found the pantothenate/CoA pathway was the most enriched pathway in the Tc22 subset (Figure 2A). This pathway produces the metabolic cofactor CoA from pantothenate (vitamin B5) through a series of metabolic intermediates. The intracellular levels of many of these intermediates were decreased in Tc22s, while CoA levels were elevated, thereby suggestive of an increased flux of pantothenate to generate CoA (Figure 2B). Hypothesizing that the pantothenate-CoA pathway may therefore facilitate the oxidative metabolic phenotype linked to the Tc22 lineage, we added exogenous pantothenate during Tc22 polarization and noted enhanced IL-22 production in both mouse (Figures 2C and 2D) and human (Figures 2E and 2F) $CD8^+$ T cells. These data indicated that pantothenate metabolism can be targeted to enhance IL-22 production in Tc22 cells.

Exogenous CoA induces OXPHOS and Tc22 polarization in the absence of polarizing cytokines

As several steps are required to generate CoA from pantothenate, we tested if the end product of the synthetic pathway, CoA, was more effective in inducing IL-22 production. CoA itself provides an attractive target in this context, given that evidence indicates augmented levels of extracellular CoA can enhance intracellular pools of CoA (Srinivasan et al., 2015). Indeed, we observed that the addition of exogenous CoA during Tc22 polarization enhanced IL-22 production to a greater extent than pantothenate (Figures 3A and 3B). Exogenous CoA also resulted in increased production of IL-2, another cytokine expressed at high levels by the Tc22 lineage (St Paul et al., 2020) (Figures 3A and 3B). Surprisingly, we found that $CD8^+$ T cells activated in the presence of CoA alone resulted in skewing toward the Tc22 phenotype as evident by enhanced IL-22 and IL-2 production (Figures 3C and 3D). RNA sequencing of these cells revealed that, similar to Tc22 cells, CoA-treated cells also did not display altered metabolic gene expression profiles (Figure S4). When comparing gene expression profiles of CoA-treated cells to Tc22 cells, we found both cell types to highly express genes that constitute the core Tc22 signature (Figure 3E). These genes include granzyme C and D, as well as the cytokine IL23a and other genes such as Lum and Ramp3, which we found to be highly expressed in Tc22s relative to other Tc subsets (Table S1). Furthermore, many of the most highly upregulated genes in Tc22 cells were also highly upregulated by CoA (Figure 3F). Therefore, activating $CD8^+$ T cells in the presence of CoA induced a cytokine and transcriptional profile resembling that of Tc22 cells despite the absence of polarizing cytokines.

Given that we demonstrated IL-22 production to be linked to the oxidative metabolism of Tc22 cells, we next tested whether CoA was able to metabolically reprogram $CD8^+$ T cells to enhance OXPHOS. Indeed, Seahorse analysis revealed CoA-treated T cells displayed enhanced oxidative metabolism (Figure 3G) with a corresponding increase in ATP (Figure 3H). Moreover, CoA metabolically reprogramed previously activated effector T cells to induce IL-22 production and OXPHOS following a subsequent stimulation in the presence of CoA (Figures S5A–S5E). The effects of CoA were not only limited to $CD8^+$ T cells, as $CD4^+$ Th22s were also dependent on OXPHOS for IL-22 production (Figure S5F) and CoA similarly induced and enhanced IL-22 production in $CD4^+$ T cells in conjunction with the metabolic shift toward OXPHOS and enhanced ATP production (Figures S5G–S5K). Taken together, these findings indicate that CoA acts on $CD4^+$ and $CD8^+$ T cells to induce an oxidative metabolic program that drives IL-22 production independent of polarizing cytokines.

To begin to investigate how CoA induced metabolic reprogramming and IL-22 production in T cells, we first aimed to rule out that CoA was acting indirectly by altering the function of the antigen presenting cells (APCs) used to activate the T cells. We confirmed that CoA was able to induce and enhance Tc22 polarization in purified T cells activated in the absence of APCs

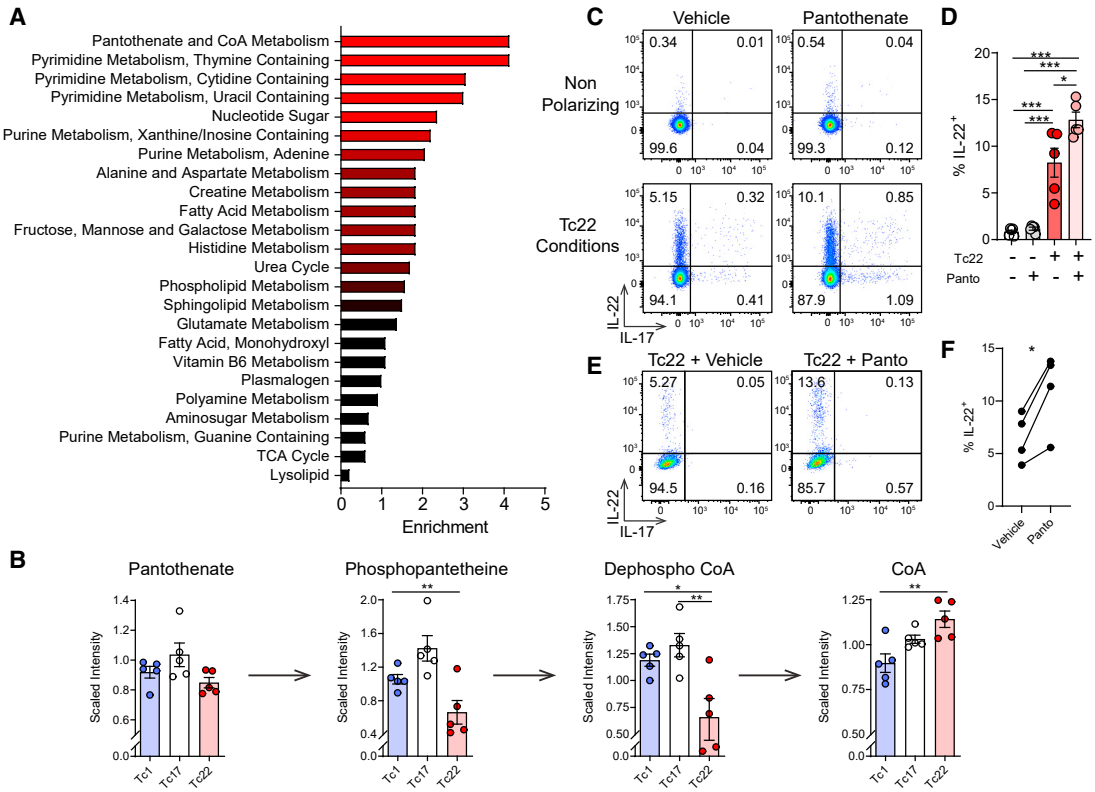

Figure 2. Pantothenate metabolism is enriched in Tc22 cells and enhances IL-22 production

(A) Metabolic pathways enriched in CD8$^+$ Tc22s as determined by mass spectrometry.

(B) Quantification of pantothenate pathway metabolites in Tc subsets. Results shown are mean scaled intensity of metabolites as determined by mass spectrometry ± SEM (n = 5).

(C and D) Cytokine expression in mouse CD8$^+$ T cells activated in non-polarizing or Tc22 polarizing conditions plus vehicle or pantothenate (n = 5 ± SEM).

(E and F) Cytokine expression in human CD8$^+$ T cells activated in Tc22 conditions plus vehicle or pantothenate (n = 4).

Results shown are representative of at least 3 independent experiments (C and E) or pooled from multiple independent experiments (D and F). Statistical significance was calculated using (B and D) ANOVA with Sidak post hoc test or (F) paired t test. *p < 0.05, **p < 0.01, ***p < 0.001.

(Figure S6A). Similarly, we confirmed that CoA was not altering the phenotype of the T cells through the production of the Tc22 polarizing cytokine IL-6, as CoA induced IL-22 production despite the presence of IL-6 neutralizing antibodies (Figure S6B). CoA also contains an adenosine moiety and can be hydrolyzed extracellularly to generate phosphopantetheine and 3′,5′-ADP (Naquet et al., 2020). Extracellular ADP, as well as ATP, can be further metabolized by ecto-enzymes to AMP and subsequently adenosine, all of which can bind P2 receptors and influence cell function (Dwyer et al., 2020). Recently, activation of the P2RX7 receptor by extracellular ATP has been shown to be important in inducing the metabolic reprogramming in CD8$^+$ memory T cells (Borges da Silva et al., 2018). Accordingly, we tested if provision of extracellular ATP could induce the same phenotypic changes as extracellular CoA. We found that unlike CoA, which enhanced Tc22 polarization, extracellular ATP inhibited Tc22 polarization (Figure S6C). Collectively, these observations led us to conclude that it was not via the generation of extracellular adenosine metabolites, nor via the modulation of APC function, nor via increased IL-6 levels that CoA was affecting T cell metabolism and function. Therefore, we sought to further interrogate the intracellular changes in global metabolism induced by CoA to attempt to gain mechanistic insight into how CoA was driving T cell metabolism and function.

Oxidative HIF and AhR signaling are required for CoA-dependent IL-22 production

To further explore the changes in intracellular metabolites caused by CoA, we utilized targeted metabolomics to determine the intracellular levels of over 100 metabolites in T cells that were activated in the presence of CoA. We discovered that treatment with CoA altered the global metabolic profile leading to alterations in metabolites involved in multiple pathways (Figure 4A). These included metabolites in pyrimidine metabolism, such as orotic acid and uracil, as well as purine metabolism, such as xanthosine and allantoic acid (Figure 4B). This suggests that treatment with CoA is inducing a metabolic program similar to Tc22 cells, as pyrimidine and purine metabolic pathways were among the most enriched in Tc22 cells (Figure 2A). Treatment with CoA also affected the CoA-pantothenic acid metabolic pathway, as pantothenic acid was highly enriched by CoA treatment (Figure 4B). This is different than what was observed for Tc22 cells, as pantothenate levels were slightly decreased in Tc22 cells but CoA levels were increased, indicating a flux of pantothenate to CoA. Both CoA

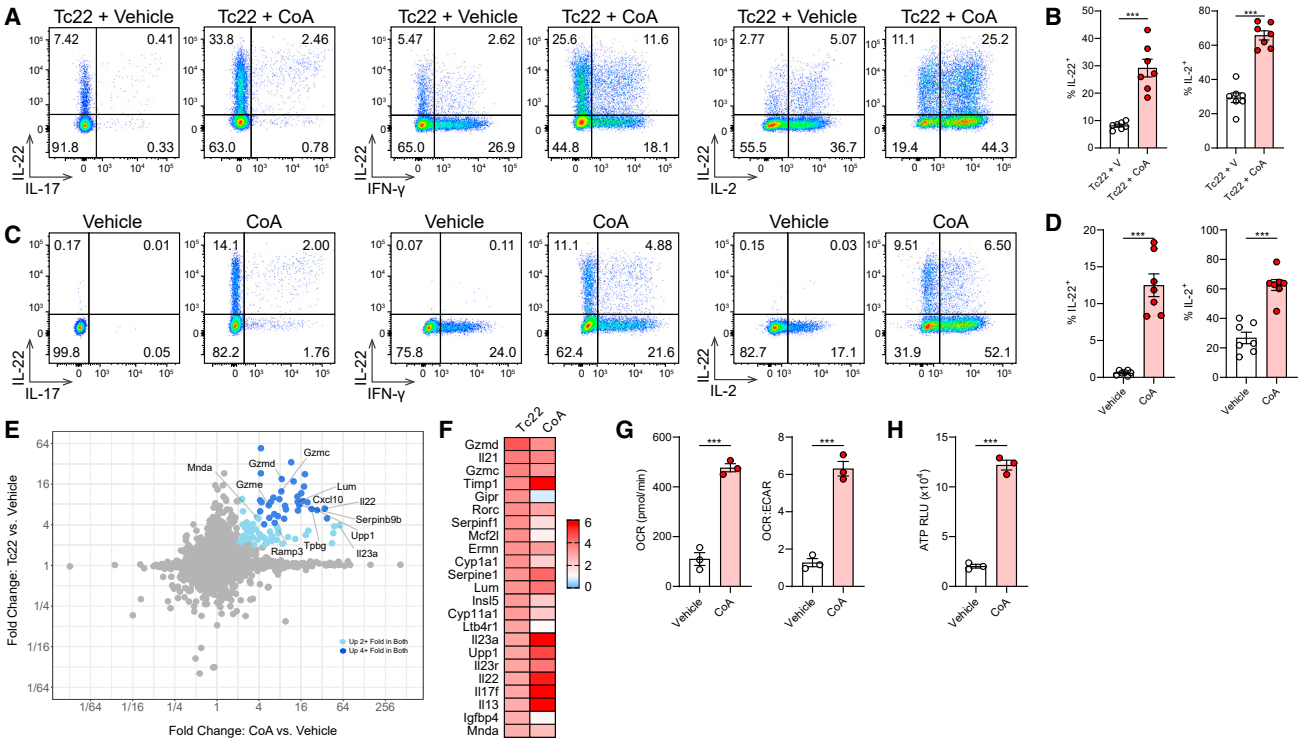

Figure 3. Coenzyme A induces Tc22 cells and OXPHOS in the absence of polarizing conditions

(A) Cytokine expression in CD8$^+$ T cells activated in Tc22 conditions plus vehicle or CoA for 3 days.

(B) Mean percent (%) IL-2- and IL-22-positive CD8$^+$ T cells activated in Tc22 conditions plus vehicle (V) or CoA pooled from 5 independent experiments (n = 7 ± SEM).

(C) Cytokine expression in CD8$^+$ T cells activated in non-polarizing conditions plus vehicle or CoA.

(D) Mean percent (%) IL-2- and IL-22-positive CD8$^+$ T cells activated in the presence of vehicle or CoA pooled from 7 independent experiments (n = 7 ± SEM).

(E and F) RNA sequencing was performed on CD8$^+$ T cells activated in the presence of Tc22 cytokines, CoA, and vehicle from 3 mice.

(E) Scatterplot comparing mean fold change gene expression of CoA/vehicle to Tc22/vehicle as determined by RNA sequencing.

(F) Expression level of top significantly upregulated genes in Tc22s. Values are expressed as mean fold change relative to vehicle-treated control cells on a log2 scale.

(G) Basal OCR and OCR:ECAR ratio quantified by Seahorse of CD8$^+$ T cells activated in the presence of vehicle or CoA (n = 3 ± SEM).

(H) ATP levels in CD8$^+$ T cells activated for 3 days in the presence of CoA or vehicle control (n = 3 ± SEM).

Results shown are representative of at least 3 independent experiments (A, C, G, and H). Statistical significance was calculated with two-tailed t test. ***$p < 0.001$.

and acetyl-CoA (AcCoA) have been reported to be allosteric inhibitors of the PANK kinases, which are responsible for phosphorylating pantothenate early in the CoA synthesis pathway (Vallari et al., 1987). Thus, the elevated levels of pantothenate suggest that treatment with CoA is increasing intracellular levels of CoA and/or AcCoA, which in turn are inhibiting the phosphorylation of pantothenate. It has also recently been demonstrated that in CD8$^+$ T cells the vast majority of intracellular AcCoA is found in the mitochondrial compartment and is utilized for mitochondrial oxidative metabolism (Vodnala et al., 2019). Therefore, we hypothesized that not only would treatment with CoA increase intracellular CoA and AcCoA levels, which causes inhibition of the PANK kinases and the accumulation of pantothenate, but that the enhanced AcCoA levels directly support the oxidative metabolic program observed in CoA-treated cells. Accordingly, we quantified the amount of total AcCoA and found that treatment with CoA greatly increased the amount of intracellular AcCoA (Figure 4C). These data suggest that treatment with CoA results in an oxidative metabolic phenotype by increasing the amount of AcCoA available in the mitochondria for the TCA cycle.

AcCoA is generated in the mitochondria via the decarboxylation of pyruvate. Given that we observed increased AcCoA levels in cells treated with CoA as well as enhanced oxidative metabolism, we wanted to assess if this was due to increased incorporation of glucose-derived pyruvate into AcCoA and the TCA cycle. To assess this, we employed stable isotope tracer analysis (SITA) with ^{13}C-glucose to interrogate the effects of CoA on glucose utilization and levels of metabolites involved in OXPHOS and the TCA cycle. We found that CoA treatment resulted in enhanced incorporation of the ^{13}C label into pyruvate and the downstream TCA metabolites such as citrate, consistent with an increased flux of glucose-derived pyruvate into the TCA cycle (Figure 4D). We noted comparable levels of ^{13}C incorporation into lactate between cells treated with CoA and the controls, indicating that CoA was not enhancing the flux of glucose-derived carbon to lactate and thus the effect of CoA was specifically enhancing mitochondrial utilization of pyruvate. Collectively, these findings are consistent with CoA treatment leading to increased generation of mitochondrial AcCoA as a result of increased flux of glucose-derived pyruvate into the

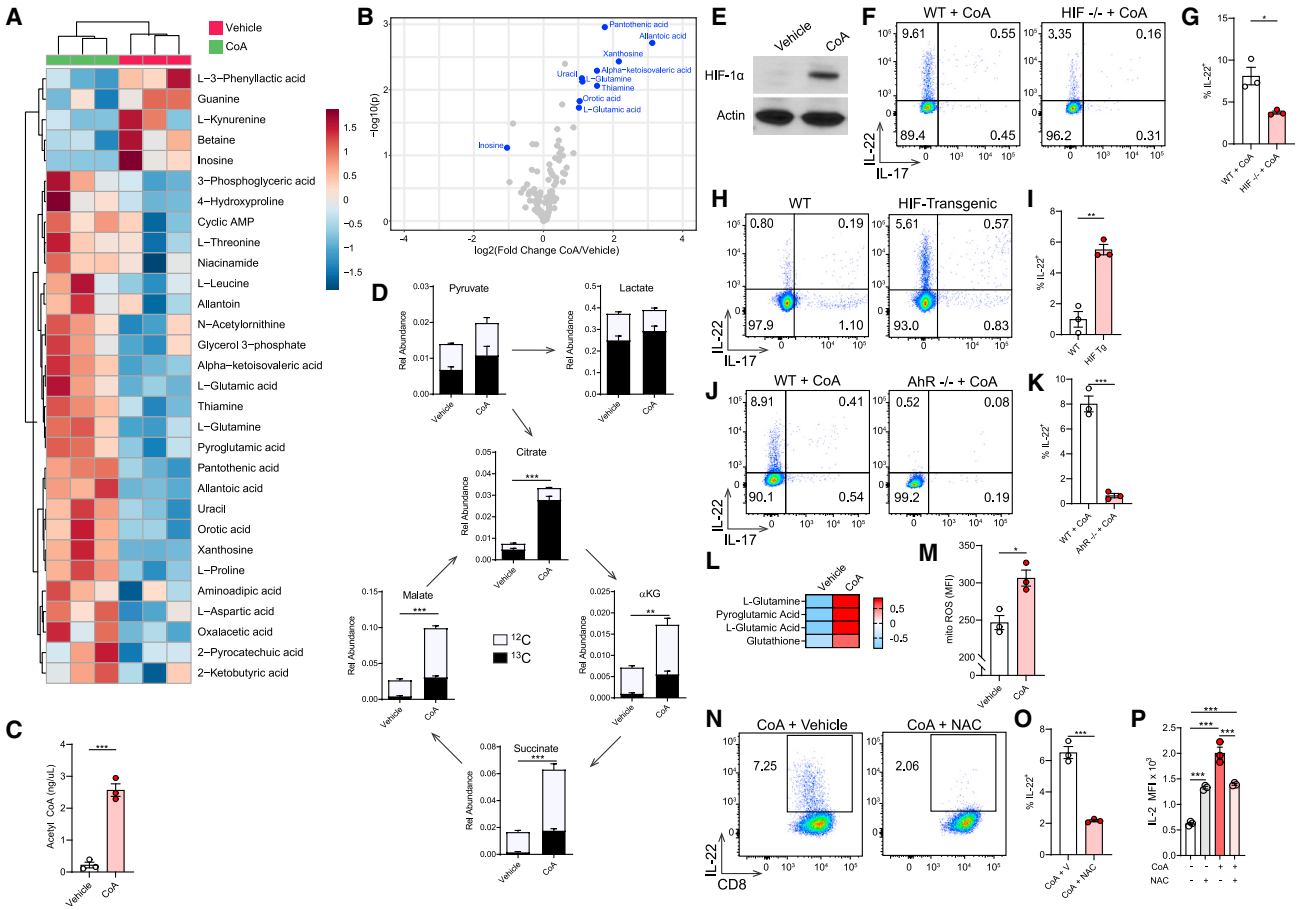

Figure 4. CoA induces IL-22 production via HIF-1α and aryl hydrocarbon receptor signaling

(A and B) CD8$^+$ T cells were activated for 3 days in the presence of CoA or vehicle and metabolites were analyzed with mass spectrometry (n = 3 mice).
(A) Heatmap of top 30 differentially regulated metabolites. Values represent *Z* score.
(B) Volcano plot highlighting most differentially regulated metabolites by CoA.
(C) Acetyl-CoA quantification in CoA- or vehicle-treated T cells (n = 3 ± SEM).
(D) CD8$^+$ T cells activated for 3 days in presence of CoA or vehicle were incubated for 2.5 h in media containing ^{13}C glucose and analyzed by mass spectrometry. Results shown are mean relative abundance of metabolites in T cells pooled from n = 3 mice ± SEM.
(E) Western blotting for HIF-1α and actin in CD8$^+$ T cells activated in the presence of vehicle or CoA.
(F) Cytokine expression in WT or HIF$^{-/-}$ CD8$^+$ T cells that were activated in the presence of CoA.
(G) Percent (%) IL-22-positive WT or HIF$^{-/-}$ CD8$^+$ T cells activated in the presence of CoA pooled from multiple independent experiments (n = 3 ± SEM).
(H) Cytokine production in WT or HIF-transgenic CD8$^+$ T cells that were activated for 3 days in non-polarizing conditions using anti-CD3 and anti-CD28.
(I) Percent (%) IL-22-positive WT or HIF-transgenic (Tg) CD8$^+$ T cells activated as in (H) pooled from multiple independent experiments (n = 3 ± SEM).
(J) Cytokine production in WT or AhR$^{-/-}$ CD8$^+$ T cells activated for 3 days in the presence of CoA.
(K) Percent (%) IL-22-positive WT or AhR$^{-/-}$ CD8+ T cells activated in the presence of CoA pooled from multiple independent experiments (n = 3 ± SEM).
(L) *Z* score of metabolites involved in ROS buffering as determined by mass spectrometry from (A).
(M) Mitochondrial ROS geometric mean fluorescence intensity (MFI) in CD8$^+$ T cells activated in the presence of vehicle or CoA as determined by flow cytometry (n = 3 ± SEM).
(N) IL-22 production in CD8$^+$ T cells activated in the presence of CoA and either vehicle control or N-acetyl-L-cysteine (NAC).
(O) Percent (%) IL-22-positive CD8+ T cells activated in the presence of CoA and either vehicle or NAC (n = 3 ± SEM).
(P) Geometric MFI of IL-2 in T cells activated in the indicated conditions (n = 3 ± SEM).
Results shown are representative of at least 2 independent experiments (C, E, F, H, J, and M–P). Statistical significance was calculated with two-tailed t test, except for (P), which used ANOVA with Sidak test. *p < 0.05, **p < 0.01, ***p < 0.001.

mitochondria and thus provide a potential mechanism to explain the increased OXPHOS observed in cells treated with CoA.

Our data, however, also indicated that this increased OXPHOS is linked to the production of IL-22. Therefore, further studies were done to explore the potential mechanistic links between the TCA cycle and IL-22 production. Interestingly, both the Tc22 cells and the CoA-treated cells had increased levels of TCA cycle intermediates, particularly succinate (Figures S2G and 4D). It has previously been demonstrated that succinate can stabilize and activate the transcription factor hypoxia inducible factor (HIF)-1α under normal oxygen tension (Selak et al., 2005; Tannahill et al., 2013), and that activation of

HIF-1α can promote IL-22 production in CD4$^+$ T cells (Budda et al., 2016). Therefore, we hypothesized that the mechanistic link between OXPHOS and the induction of IL-22 expression was the succinate-induced activation of HIF-1α signaling in an oxygen-replete environment, so-called oxidative HIF-1α. Consistent with this hypothesis, we noted increased levels of HIF-1α protein in CoA-treated T cells (Figure 4E), and HIF-1α-deficient T cells had impaired IL-22 production following treatment with CoA (Figures 4F and 4G). A similar finding was observed when blocking HIF-1α activity pharmacologically (Figure S6D). Moreover, activation of CD8$^+$ T cells that constitutively express HIF-1α (Kim et al., 2006) induced IL-22 production (Figures 4H and 4I), and activation of CD8$^+$ T cells in the presence of cell-permeable succinate induced IL-22 production (Figure S6E). However, it is important to note that blockade of HIF-1α did not completely abrogate IL-22 production, suggesting other mechanisms are involved. Indeed, in Tc22 cells the aryl hydrocarbon receptor (AhR) transcription factor was also found to mediate polarization (St Paul et al., 2020). When blocking AhR activity pharmacologically (Figure S6F) or when using T cells from AhR$^{-/-}$ mice (Figures 4J and 4K), the ability for CoA to induce IL-22 production in T cells was diminished. These findings demonstrate that CoA requires the activation of both HIF-1α and the AhR to fully induce IL-22 production.

Activation of the AhR typically occurs following binding of ligands such as those derived from tryptophan (Veldhoen and Duarte, 2010). Recently, it has been reported that metabolites such as reactive oxygen species (ROS) may also lead to AhR activation (Kubli et al., 2019). We further examined the metabolic data from CoA-treated cells and found increased levels of metabolites associated with ROS buffering, such as glutathione (Figure 4L). Given that ROS production is linked to the utilization of OXPHOS, we investigated if there was enhanced mitochondrial ROS production in cells treated with CoA. Indeed, we confirmed increased mitochondrial ROS production in the CoA-treated T cells (Figure 4M). To determine whether this increased ROS was important for AhR activation and subsequent IL-22 production, we activated CD8$^+$ T cells with CoA in the presence of the ROS inhibitor N-acetyl-L-cysteine (NAC) and observed a significant decrease in IL-22 production (Figures 4N and 4O). NAC also inhibited IL-2 production by CoA-treated cells, while conversely, NAC enhanced IL-2 production in T cells activated in the absence of CoA, consistent with previous reports (Pilipow et al., 2018) (Figure 4P). Collectively, these findings demonstrate that CoA activates HIF-1α and AhR to induce IL-22 production. Furthermore, these data indicated that IL-22 production is driven downstream of the oxidative metabolic phenotype induced by CoA via the generation of metabolic intermediates that activate HIF-1α and AhR. Therefore, these findings establish that a single metabolite, CoA, can metabolically reprogram CD8$^+$ T cells to induce cells that are functionally, metabolically, and transcriptionally similar to Tc22 cells independent of polarizing cytokines.

CoA enhances anti-tumor activity and persistence of CD8+ T cells

Our original hypothesis was that the metabolic programming of Tc22 cells was responsible for both their IL-22 production and their enhanced anti-tumor function, but the metabolic phenotype underpinned their ability to control tumor growth. We have found that oxidative metabolism downstream of the pantothenate-CoA pathway is responsible for the IL-22 production in Tc22 cells. Recent reports in the literature have linked CD8$^+$ T cells with increased capacity for OXPHOS with enhanced anti-tumor responses (Buck et al., 2016; Crompton et al., 2015; Saibil et al., 2019; Scharping et al., 2016). Given that treatment with CoA recapitulated the Tc22 phenotype metabolically with increased OXPHOS and bioenergetics, we evaluated whether metabolically reprogramming CD8$^+$ T cells with CoA resulted in enhanced immunotherapeutic responses in mouse tumor models. LCMV gp tumor-specific P14 CD8$^+$ T cells, activated for 3 days in the presence of vehicle or CoA, were transferred into mice inoculated with B16 melanoma tumors that expressed the LCMV-gp33 peptide. Mice that received CoA-treated CD8$^+$ P14 T cells demonstrated a significantly greater reduction in tumor growth compared to animals that received activated CD8$^+$ P14 T cells treated with vehicle (Figures 5A and 5B). Next, we tested whether CoA-treated T cells can control well-established tumors in a mouse model resistant to immunotherapy. Here, we used the RIP-GP SV40 spontaneous tumor model in which mouse β islet cells express both the large T antigen from SV40 and the LCMV Gp protein (Dissanayake et al., 2011a). Tumor burden can be continuously assessed by measuring peripheral blood glucose, as an increase in tumor size leads to elevated insulin, which thereby decreases blood glucose levels. When mice develop large established tumors causing hypoglycemia (<5 mM blood glucose), they received CoA-treated or vehicle-treated tumor-specific CD8$^+$ P14 T cells. Mice receiving CoA-treated T cells had better tumor control as evident by both a stabilization of blood glucose (Figure 5C) and prolonged survival (Figure 5D). In contrast, the mice receiving vehicle-treated cells failed to mount a significant anti-tumor response and did not survive longer than mice who did not receive T cells. Moreover, a greater number of transferred CoA-treated T cells could be detected in the tumor draining lymph node 18 days post-transfer compared with vehicle-treated T cells (Figure 5E). This indicated CoA treatment enhanced persistence or expansion of the transferred T cells. The increased number of P14 cells treated with CoA correlated with increased IL-2, but not IFN-γ, production (Figures 5F and 5G). This phenotype resembles their cytokine profile prior to transfer (Figure 3C). Together, these findings demonstrate that treatment with CoA can enhance the anti-tumor function of T cells in adoptive cell therapy models.

Pantothenate increases responses to immunological checkpoint blockade

Enhancing T cell oxidative metabolism has been shown to be a promising strategy to improve response rates to immunological checkpoint blockade therapies such as those targeting the PD1 axis (Chamoto et al., 2017). To this end, we tested whether targeting the pantothenate pathway *in vivo* could synergize with anti-PDL1 therapy. Given the fact that injected CoA is not stable *in vivo* (Srinivasan et al., 2015), we administered pantothenate or vehicle to mice bearing established MC-38 tumors in conjunction with anti-PDL1 therapy (Figures 6A–6C). We found that mice that received pantothenate had an overall reduction in tumor growth (Figure 6A), with a significant reduction in tumor

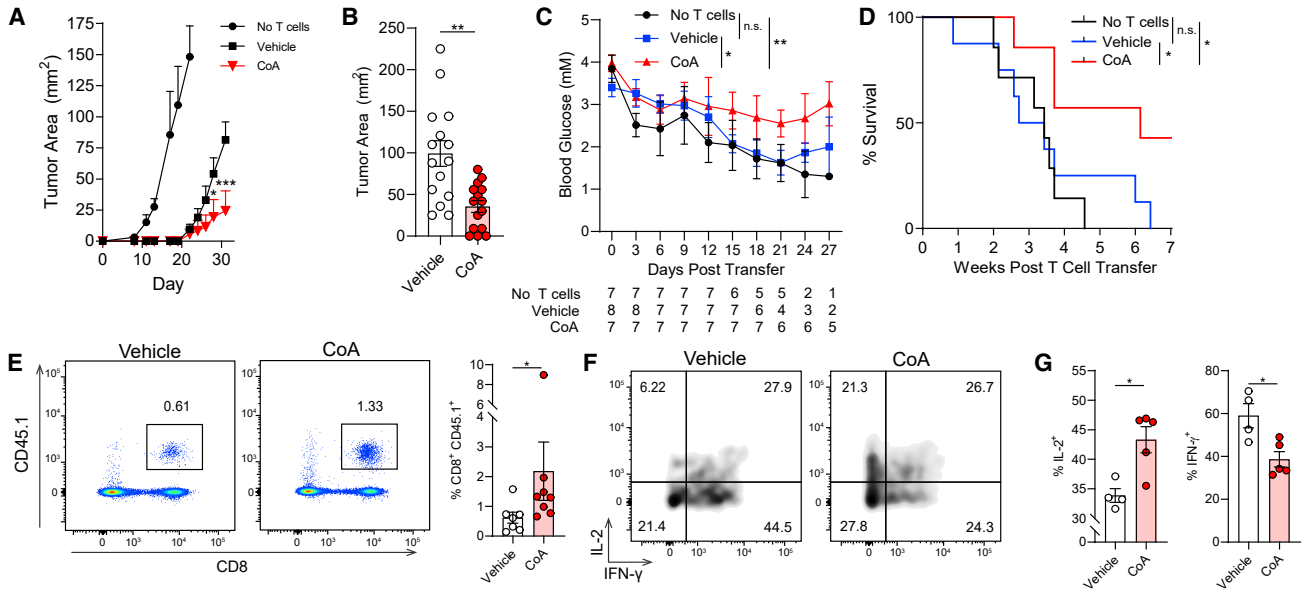

Figure 5. CoA enhances T cell anti-tumor function

(A and B) Mice were inoculated with B16-gp33 melanoma tumors and concurrently received an adoptive transfer of 0.5 × 10^6 $CD8^+$ $P14^+$ gp33-specific T cells activated in the presence of CoA or vehicle.

(A) Results shown are mean tumor area (LxW) of 5 mice/group ± SEM.

(B) Cumulative mean tumor area from (A) on day 31 pooled from 3 independent experiments (n = 15 mice/group ± SEM).

(C–F) Mice bearing well-established spontaneous pancreatic tumors received 1.5 × 10^6 tumor-specific $CD8^+$ $P14^+$ T cells activated *in vitro* in the presence of CoA or vehicle control.

(C) Blood glucose was measured regularly in mice after adoptive transfer (n = numbers below ± SEM). A decrease in blood glucose correlates with an increase in tumor burden.

(D) Survival curve from (C).

(E) Percent (%) of transferred T cells ($CD45.1^+$) in the tumor draining lymph node 18 days post-transfer (n = 7–8 ± SEM).

(F) Cytokine production in transferred $CD45.1^+$ $CD8^+$ T cells within the tumor draining lymph node 18 days post-transfer.

(G) Percent (%) of transferred $CD45.1^+$ $CD8^+$ T cells from (F) producing IL-2 or IFN- γ (n = 4–5 ± SEM).

Results shown are representative of 2–3 independent experiments (A, F, and G) or pooled from multiple independent experiments (B–E). Two-way ANOVA with Sidak test (A and C), Mann-Whitney U test (B, E, and G), and log-rank test (D) were used to calculate statistical significance. *p < 0.05, **p < 0.01, ***p < 0.001; n.s., not significant.

burden observed on day 28 post-tumor inoculation (Figure 6B). This led to a corresponding increase in overall survival in addition to curative complete responses observed in some mice that received pantothenate, but not vehicle-treated controls (Figure 6C). Therefore, these findings indicate that the *in vivo* administration of pantothenate can enhance response rates to anti-PDL1 in a murine tumor model.

Given these findings, we tested whether pantothenate could be associated with responses to anti-PD1 therapy in humans. Using mass spectrometry, we detected over 100 different metabolites in plasma samples from 42 patients with Stage III or Stage IV melanoma prior to these patients receiving anti-PD1 antibody therapy (21 responders and 21 non-responders). Pantothenic acid was the most enriched metabolite in patients who demonstrated response to anti-PD1 therapy (Figure 6D). A waterfall plot analysis revealed that patients with the top 1/3 of pantothenic acid plasma levels were mostly responders, whereas the bottom 1/3 of patients contained equal numbers of both responders and non-responders (Figure 6E). This is suggestive of a threshold effect in which a certain threshold level of plasma pantothenic acid must be reached to derive clinical benefit. In support of this, we found that patients with the highest plasma pantothenic acid levels demonstrated a significantly longer time to next treatment (TTNT) compared to patients with lower levels (Figure 6F). Additionally, we found that melanoma patients responding to anti-PD1 therapy upregulated many genes associated with the Tc22 lineage (Figures 3E and 3F), including IL-22 (Figure 6G), as determined by re-analyzing a previously published dataset of gene expression profiles of on-treatment tumor biopsies from a different cohort of patients (Chen et al., 2016). Together, these findings suggest an important role for pantothenate metabolism in influencing the response to PD-1 checkpoint blockade.

DISCUSSION

The importance of metabolites in modulating immune function and immunotherapeutic responses is beginning to be appreciated. We investigated the metabolic phenotypes of $CD8^+$ T cells polarized to the Tc1, Tc17, and Tc22 lineages to identify metabolic pathways associated with robust anti-tumor responses observed in Tc22 cells. We found that Tc22 cells displayed enhanced oxidative metabolism and upregulated the pantothenate/CoA metabolic pathway. By treating T cells with

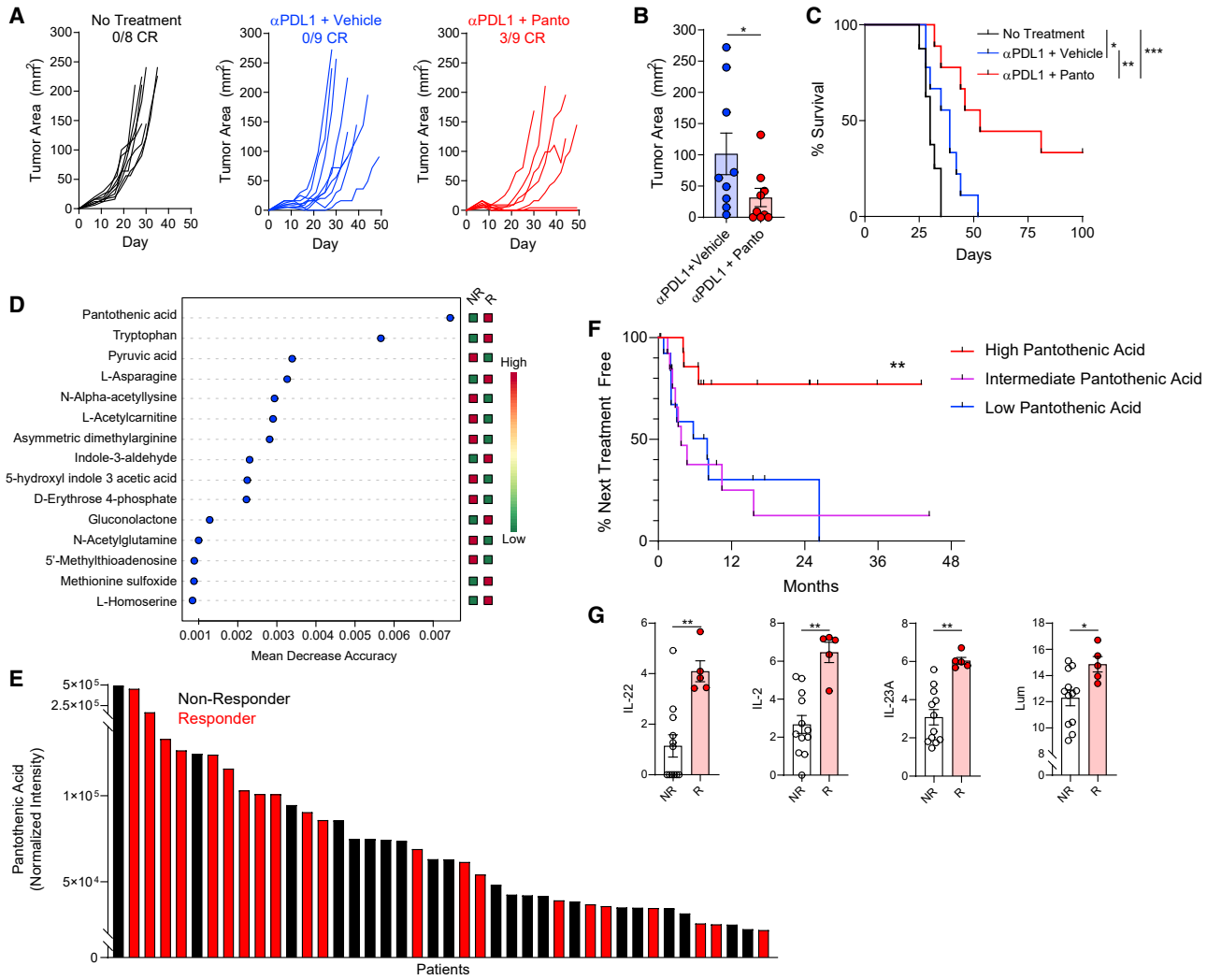

Figure 6. Pantothenate enhances responses to immunological checkpoint blockade

(A–C) Mice bearing day 7 established MC-38 tumors were treated with anti-PDL1 in conjunction with pantothenate (Panto) or vehicle control delivered intraperitoneally.

(A) Tumor curves representing tumor growth of mice treated as indicated pooled from multiple independent experiments (n = 8–9 mice per group; CR, complete responder).

(B) Pooled tumor area on day 28 post-tumor inoculation (n = 9 per group).

(C) Survival curve from (A) pooled from multiple independent experiments (n = 8–9 mice per group).

(D–F) Plasma was collected from human melanoma patients (n = 42, 21 responders and 21 non-responders) prior to administration of anti-PD1 antibody therapy and analyzed with mass spectrometry.

(D) Variable importance plot indicating pantothenic acid as the metabolite most enriched in responders (NR, non-responder; R, responder).

(E) Waterfall plot indicating pantothenic acid levels in each patient with their response status.

(F) Time to next treatment curve of patients stratified into tertiles based on levels of pre-treatment plasma pantothenic acid (n = 14 patients per tertile). Time represents months from start of anti-PD1 therapy.

(G) Nanostring RNA sequencing analysis from a previously published dataset indicating Tc22 genes as being upregulated in on-treatment tumor biopsies of responders to anti-PD1 antibody therapy.

Mann-Whitney U test (B and G) and log-rank test (C and F) were used to calculate statistical significance. *p < 0.05, **p < 0.01, ***p < 0.001.

CoA, a single metabolite administered exogenously, we could metabolically and functionally reprogram a T cell to increase mitochondrial metabolism and bioenergetics and adopt the Tc22 phenotype. Importantly, we found that this reprogramming increases the anti-tumor efficacy of these cells in two adoptive cell therapy models. We also found that administration of pantothenate increased the efficacy of anti-PD-L1 therapy in a murine model. These data were echoed in a cohort of melanoma patients as we observed a correlation between high plasma pantothenic acid and response to PD-1 blockade. These data identify a previously unappreciated role for pantothenic acid metabolism in influencing anti-tumor immunity.

Differentiation of $CD4^+$ T cells and $CD8^+$ T cells into Th/Tc subsets is mediated by polarizing cytokines and lineage-specific

transcription factors. Accompanying this transcriptional and functional lineage commitment is a metabolic reprogramming that helps to facilitate polarization. For instance, Th17 cells rely on *de novo* fatty acid synthesis to generate short-chain fatty acids that can stabilize the master-regulator transcription factor RORγt (Berod et al., 2014; Wang et al., 2015). Interfering with the fatty acid synthesis pathway not only inhibits the generation of Th17, but also promotes differentiation into regulatory T cells (Berod et al., 2014). In addition to fatty acid synthesis, Th17 cells also rely on increased glutathione production to inhibit ROS, and interfering with glutathione production by targeting glutaminase can selectively inhibit Th17 cells, but not Th1 cells (Johnson et al., 2018). Together, these findings highlight the importance of metabolism in governing T cell subset differentiation. However, it is important to note that T cells in these studies were activated in the presence of polarizing cytokines, and it is unclear whether the metabolic shift alone downstream of polarizing cytokines is sufficient to drive lineage commitment. Our data suggest that in the case of the Tc22 subset, the metabolic reprogramming toward oxidative metabolism can re-capitulate the Tc22 metabolic, effector, and transcriptional phenotype mediated in part by the Tc22 "master regulator" transcription factor AhR. Although we propose that CoA is being used as a substrate to generate TCA metabolites such as AcCoA that fuel OXPHOS and activate HIF and AhR transcription factors, we cannot conclusively rule out that CoA is acting through an undefined surface receptor to upregulate oxidative metabolism and TCA cycle metabolites through other means. Nevertheless, our data show that increased OXPHOS is critical to the induction of Tc22, and induction of OXPHOS with the exogenous administration of CoA can recapitulate the Tc22 phenotype in the absence of polarizing cytokines, therefore identifying a novel method for T cell subset induction.

T cell metabolism and effector function are intricately linked, and recent efforts have been aimed at enhancing anti-tumor function of T cells via metabolic reprogramming. Tumor infiltrating lymphocytes and exhausted T cells display a metabolic profile consistent with decreased mitochondrial activity as indicated by a reduction in OCR and mitochondrial mass (Bengsch et al., 2016; Scharping et al., 2016). As a result, it has been shown that enhancing OXPHOS and mitochondrial metabolism can render T cells less susceptible to exhaustion and immunosuppressive activity within the tumor microenvironment to enhance anti-tumor activity (Scharping et al., 2016). In addition to enhancing effector function, increased mitochondrial metabolism and OXPHOS have also been shown to enhance T cell persistence and expansion (Saibil et al., 2019). Together, these previous findings support our current study as we identified CoA as a reagent to enhance OXPHOS in T cells leading to increased IL-2 and persistence following transfer, culminating in enhanced anti-tumor activity in multiple mouse models. In addition to enhancing cell therapy protocols, we also identified the CoA pre-cursor pantothenate as a reagent to enhance response to anti-PDL1 in mouse models and correlated pre-treatment plasma pantothenic acid levels with response to checkpoint blockade in human patients with advanced melanoma. Interestingly, one source of pantothenic acid in humans is from the microbiome (Magnúsdóttir et al., 2015). Recent reports have identified a link between the microbiome and response to anti-PD1 therapy; however, the mechanisms remain unclear (Gopalakrishnan et al., 2018; Routy et al., 2018; Sivan et al., 2015). Based on our present findings, it is possible that pantothenic acid may be one link between the microbiome and response to anti-PD1 therapy and should be further explored.

In conclusion, we demonstrate the importance of the pantothenate/CoA pathway in the metabolic reprogramming of T cells to enhance their anti-tumor activity in multiple mouse models. Together, these findings provide the rationale for further work to see if manipulation of this pathway can be leveraged to increase the efficacy of both adoptive cellular therapies and immune checkpoint blockade in the clinic.

Limitations of study

Although we were able to demonstrate profound functional, transcriptional, and metabolic changes induced by the addition of exogenous CoA, we were unable to directly track the fate of the exogenous CoA in order to further elucidate the mechanism of its effect. Our data support a model in which the exogenous CoA resulted in an increased mitochondrial pool of AcCoA that fueled oxidative metabolism. This OXPHOS in turn led to the activation of AhR and HIF-1α downstream of ROS and succinate, respectively. Unfortunately, we were not able to obtain labeled CoA to directly demonstrate that the exogenous CoA directly fed into the mitochondria AcCoA pool. Another limitation was with respect to the human metabolomics data. The data correlating pre-treatment plasma pantothenic acid levels with response to anti-PD1 therapy are retrospective in nature and from a relatively small cohort of patients treated at a single center. These data need to be validated in a prospective manner in a larger patient cohort.

STAR★METHODS

Detailed methods are provided in the online version of this paper and include the following:

- KEY RESOURCES TABLE
- RESOURCE AVAILABILITY
  - Lead contact
  - Materials availability
  - Data and code availability
- EXPERIMENTAL MODEL AND SUBJECT DETAILS
  - Animals
  - Human subjects
  - Cell lines
- METHOD DETAILS
  - Tc Subset polarization
  - Flow cytometry and antibodies
  - Metabolomic profiling
  - Metabolic assays
  - Stable isotype tracing analysis
  - Pharmacologic compounds
  - RNA extraction and sequencing
  - RNA sequencing data analysis
  - Tumor experiments
  - Human T cell experiments
  - Human patient cohort
- QUANTIFICATION AND STATISTICAL ANALYSIS

SUPPLEMENTAL INFORMATION

Supplemental information can be found online at https://doi.org/10.1016/j.cmet.2021.11.010.

ACKNOWLEDGMENTS

The authors would like to thank L. Wybenga-Groot, J. Kinchen, K. Gill, C. Fladd, C. Lo, and P. Yen for their technical assistance. The authors would also like to thank B. Wang for creating the graphical abstract. Stable isotope tracing data were collected at the Metabolomics Innovation Resource (MIR) located at the Rosalind and Morris Goodman Cancer Institute (GCI) at McGill University with technical assistance from D. Avizonis and L. Choiniere. The MIR is supported by the Terry Fox Research Institute, Quebec Breast Cancer Foundation, GCI, and McGill University. Targeted metabolomic analyses were conducted at the Dalhousie Biological Mass Spectrometry Core Facility with the aid of A. Cohen. This work was supported by a Canadian Institute for Health Research Foundation Award to P.S.O. and a Natural Science and Engineering Research Council award to M.S.P. and C.W.T. S.D.S. was supported by the Eliot Phillipson Clinician Scientist Training Program and the Clinician Investigator Program at the University of Toronto. P.S.O. holds a Canada Research Chair in Autoimmunity and Tumor Immunity.

AUTHOR CONTRIBUTIONS

M.S.P., S.D.S., and P.S.O. designed and supervised the project, analyzed the data, and wrote the manuscript. S.J.H., K.I.-W., S.C.L., C.R.G.-B., M.K., C.R.-T., M.J.G., C.W.T., A.R.E., and L.T.N. assisted with experiments. R.N.A., L.E.H., and J.A.W. provided clinical samples and patient outcome data. R.C.L., S.P., and D.M.P. conducted metabolomic analysis. A.S., D.T.M., and T.J.P. conducted RNA sequencing analysis.

DECLARATION OF INTERESTS

M.S.P., S.D.S., and P.S.O. have filed for a patent pertaining to this work.

Received: July 9, 2021
Revised: September 20, 2021
Accepted: November 15, 2021
Published: December 7, 2021

REFERENCES

Ahlfors, H., Morrison, P.J., Duarte, J.H., Li, Y., Biro, J., Tolaini, M., Di Meglio, P., Potocnik, A.J., and Stockinger, B. (2014). IL-22 fate reporter reveals origin and control of IL-22 production in homeostasis and infection. J. Immunol. *193*, 4602–4613.

Bengsch, B., Johnson, A.L., Kurachi, M., Odorizzi, P.M., Pauken, K.E., Attanasio, J., Stelekati, E., McLane, L.M., Paley, M.A., Delgoffe, G.M., and Wherry, E.J. (2016). Bioenergetic insufficiencies due to metabolic alterations regulated by the inhibitory receptor PD-1 are an early driver of CD8(+) T cell exhaustion. Immunity *45*, 358–373.

Berod, L., Friedrich, C., Nandan, A., Freitag, J., Hagemann, S., Harmrolfs, K., Sandouk, A., Hesse, C., Castro, C.N., Bähre, H., et al. (2014). De novo fatty acid synthesis controls the fate between regulatory T and T helper 17 cells. Nat. Med. *20*, 1327–1333.

Borges da Silva, H., Beura, L.K., Wang, H., Hanse, E.A., Gore, R., Scott, M.C., Walsh, D.A., Block, K.E., Fonseca, R., Yan, Y., et al. (2018). The purinergic receptor P2RX7 directs metabolic fitness of long-lived memory $CD8^+$ T cells. Nature *559*, 264–268.

Buck, M.D., O'Sullivan, D., Klein Geltink, R.I., Curtis, J.D., Chang, C.H., Sanin, D.E., Qiu, J., Kretz, O., Braas, D., van der Windt, G.J.W., et al. (2016). Mitochondrial dynamics controls T cell fate through metabolic programming. Cell *166*, 63–76.

Budda, S.A., Girton, A., Henderson, J.G., and Zenewicz, L.A. (2016). Transcription factor HIF-1α controls expression of the cytokine IL-22 in CD4 T cells. J. Immunol. *197*, 2646–2652.

Chamoto, K., Chowdhury, P.S., Kumar, A., Sonomura, K., Matsuda, F., Fagarasan, S., and Honjo, T. (2017). Mitochondrial activation chemicals synergize with surface receptor PD-1 blockade for T cell-dependent antitumor activity. Proc. Natl. Acad. Sci. USA *114*, E761–E770.

Chang, C.-H., and Pearce, E.L. (2016). Emerging concepts of T cell metabolism as a target of immunotherapy. Nat. Immunol. *17*, 364–368.

Chang, C.H., Curtis, J.D., Maggi, L.B., Jr., Faubert, B., Villarino, A.V., O'Sullivan, D., Huang, S.C.C., van der Windt, G.J.W., Blagih, J., Qiu, J., et al. (2013). Posttranscriptional control of T cell effector function by aerobic glycolysis. Cell *153*, 1239–1251.

Chen, P.L., Roh, W., Reuben, A., Cooper, Z.A., Spencer, C.N., Prieto, P.A., Miller, J.P., Bassett, R.L., Gopalakrishnan, V., Wani, K., et al. (2016). Analysis of immune signatures in longitudinal tumor samples yields insight into biomarkers of response and mechanisms of resistance to immune checkpoint blockade. Cancer Discov. *6*, 827–837.

Chong, J., Yamamoto, M., and Xia, J. (2019). MetaboAnalystR 2.0: from raw spectra to biological insights. Metabolites *9*, 57.

Crompton, J.G., Sukumar, M., Roychoudhuri, R., Clever, D., Gros, A., Eil, R.L., Tran, E., Hanada, K., Yu, Z., Palmer, D.C., et al. (2015). Akt inhibition enhances expansion of potent tumor-specific lymphocytes with memory cell characteristics. Cancer Res. *75*, 296–305.

Dissanayake, D., Gronski, M.A., Lin, A., Elford, A.R., and Ohashi, P.S. (2011a). Immunological perspective of self versus tumor antigens: insights from the RIP-gp model. Immunol. Rev. *241*, 164–179.

Dissanayake, D., Hall, H., Berg-Brown, N., Elford, A.R., Hamilton, S.R., Murakami, K., Deluca, L.S., Gommerman, J.L., and Ohashi, P.S. (2011b). Nuclear factor-κB1 controls the functional maturation of dendritic cells and prevents the activation of autoreactive T cells. Nat. Med. *17*, 1663–1667.

Dwyer, K.M., Kishore, B.K., and Robson, S.C. (2020). Conversion of extracellular ATP into adenosine: a master switch in renal health and disease. Nat. Rev. Nephrol. *16*, 509–524.

Gattinoni, L., Klebanoff, C.A., and Restifo, N.P. (2012). Paths to stemness: building the ultimate antitumour T cell. Nat. Rev. Cancer *12*, 671–684.

Gerriets, V.A., Kishton, R.J., Nichols, A.G., Macintyre, A.N., Inoue, M., Ilkayeva, O., Winter, P.S., Liu, X., Priyadharshini, B., Slawinska, M.E., et al. (2015). Metabolic programming and PDHK1 control CD4+ T cell subsets and inflammation. J. Clin. Invest. *125*, 194–207.

Gopalakrishnan, V., Spencer, C.N., Nezi, L., Reuben, A., Andrews, M.C., Karpinets, T.V., Prieto, P.A., Vicente, D., Hoffman, K., Wei, S.C., et al. (2018). Gut microbiome modulates response to anti-PD-1 immunotherapy in melanoma patients. Science *359*, 97–103.

Johnson, M.O., Wolf, M.M., Madden, M.Z., Andrejeva, G., Sugiura, A., Contreras, D.C., Maseda, D., Liberti, M.V., Paz, K., Kishton, R.J., et al. (2018). Distinct regulation of Th17 and Th1 cell differentiation by glutaminase-dependent metabolism. Cell *175*, 1780–1795.e19.

Kawalekar, O.U., O'Connor, R.S., Fraietta, J.A., Guo, L., McGettigan, S.E., Posey, A.D., Jr., Patel, P.R., Guedan, S., Scholler, J., Keith, B., et al. (2016). Distinct signaling of coreceptors regulates specific metabolism pathways and impacts memory development in CAR T cells. Immunity *44*, 380–390.

Kim, W.Y., Safran, M., Buckley, M.R.M., Ebert, B.L., Glickman, J., Bosenberg, M., Regan, M., and Kaelin, W.G., Jr. (2006). Failure to prolyl hydroxylate hypoxia-inducible factor alpha phenocopies VHL inactivation in vivo. EMBO J. *25*, 4650–4662.

Kubli, S.P., Bassi, C., Roux, C., Wakeham, A., Göbl, C., Zhou, W., Jafari, S.M., Snow, B., Jones, L., Palomero, L., et al. (2019). AhR controls redox homeostasis and shapes the tumor microenvironment in BRCA1-associated breast cancer. Proc. Natl. Acad. Sci. USA *116*, 3604–3613.

Magnúsdóttir, S., Ravcheev, D., de Crécy-Lagard, V., and Thiele, I. (2015). Systematic genome assessment of B-vitamin biosynthesis suggests co-operation among gut microbes. Front. Genet. *6*, 148.

Menk, A.V., Scharping, N.E., Rivadeneira, D.B., Calderon, M.J., Watson, M.J., Dunstane, D., Watkins, S.C., and Delgoffe, G.M. (2018). 4-1BB costimulation induces T cell mitochondrial function and biogenesis enabling cancer immunotherapeutic responses. J. Exp. Med. *215*, 1091–1100.

Michalek, R.D., Gerriets, V.A., Jacobs, S.R., Macintyre, A.N., MacIver, N.J., Mason, E.F., Sullivan, S.A., Nichols, A.G., and Rathmell, J.C. (2011). Cutting edge: distinct glycolytic and lipid oxidative metabolic programs are essential for effector and regulatory CD4+ T cell subsets. J. Immunol. *186*, 3299–3303.

Mittrücker, H.-W., Visekruna, A., and Huber, M. (2014). Heterogeneity in the differentiation and function of CD8$^+$ T cells. Arch. Immunol. Ther. Exp. (Warsz.) *62*, 449–458.

Naquet, P., Kerr, E.W., Vickers, S.D., and Leonardi, R. (2020). Regulation of coenzyme A levels by degradation: the 'ins and outs'. Prog. Lipid Res. *78*, 101028.

Nguyen, L.T., Elford, A.R., Murakami, K., Garza, K.M., Schoenberger, S.P., Odermatt, B., Speiser, D.E., and Ohashi, P.S. (2002). Tumor growth enhances cross-presentation leading to limited T cell activation without tolerance. J. Exp. Med. *195*, 423–435.

O'Neill, L.A.J., Kishton, R.J., and Rathmell, J. (2016). A guide to immunometabolism for immunologists. Nat. Rev. Immunol. *16*, 553–565.

O'Sullivan, D., van der Windt, G.J.W., Huang, S.C.-C., Curtis, J.D., Chang, C.-H., Buck, M.D., Qiu, J., Smith, A.M., Lam, W.Y., DiPlato, L.M., et al. (2014). Memory CD8(+) T cells use cell-intrinsic lipolysis to support the metabolic programming necessary for development. Immunity *41*, 75–88.

Oxenius, A., Bachmann, M.F., Zinkernagel, R.M., and Hengartner, H. (1998). Virus-specific MHC-class II-restricted TCR-transgenic mice: effects on humoral and cellular immune responses after viral infection. Eur. J. Immunol. *28*, 390–400.

Pearce, E.L., Walsh, M.C., Cejas, P.J., Harms, G.M., Shen, H., Wang, L.-S., Jones, R.G., and Choi, Y. (2009). Enhancing CD8 T-cell memory by modulating fatty acid metabolism. Nature *460*, 103–107.

Pearce, E.L., Poffenberger, M.C., Chang, C.-H., and Jones, R.G. (2013). Fueling immunity: insights into metabolism and lymphocyte function. Science *342*, 1242454.

Pilipow, K., Scamardella, E., Puccio, S., Gautam, S., De Paoli, F., Mazza, E.M., De Simone, G., Polletti, S., Buccilli, M., Zanon, V., et al. (2018). Antioxidant metabolism regulates CD8+ T memory stem cell formation and antitumor immunity. JCI Insight *3*, e122299.

Pino, L.K., Searle, B.C., Bollinger, J.G., Nunn, B., MacLean, B., and MacCoss, M.J. (2020). The Skyline ecosystem: informatics for quantitative mass spectrometry proteomics. Mass Spectrom. Rev. *39*, 229–244.

Pircher, H., Bürki, K., Lang, R., Hengartner, H., and Zinkernagel, R.M. (1989). Tolerance induction in double specific T-cell receptor transgenic mice varies with antigen. Nature *342*, 559–561.

Routy, B., Le Chatelier, E., Derosa, L., Duong, C.P.M., Alou, M.T., Daillère, R., Fluckiger, A., Messaoudene, M., Rauber, C., Roberti, M.P., et al. (2018). Gut microbiome influences efficacy of PD-1-based immunotherapy against epithelial tumors. Science *359*, 91–97.

Saibil, S.D., St Paul, M., Laister, R.C., Garcia-Batres, C.R., Israni-Winger, K., Elford, A.R., Grimshaw, N., Robert-Tissot, C., Roy, D.G., Jones, R.G., et al. (2019). Activation of peroxisome proliferator-activated receptors α and δ synergizes with inflammatory signals to enhance adoptive cell therapy. Cancer Res. *79*, 445–451.

Scharping, N.E., Menk, A.V., Moreci, R.S., Whetstone, R.D., Dadey, R.E., Watkins, S.C., Ferris, R.L., and Delgoffe, G.M. (2016). The tumor microenvironment represses T cell mitochondrial biogenesis to drive intratumoral T cell metabolic insufficiency and dysfunction. Immunity *45*, 374–388.

Selak, M.A., Armour, S.M., MacKenzie, E.D., Boulahbel, H., Watson, D.G., Mansfield, K.D., Pan, Y., Simon, M.C., Thompson, C.B., and Gottlieb, E. (2005). Succinate links TCA cycle dysfunction to oncogenesis by inhibiting HIF-α prolyl hydroxylase. Cancer Cell *7*, 77–85.

Shin, S.-Y., Fauman, E.B., Petersen, A.-K., Krumsiek, J., Santos, R., Huang, J., Arnold, M., Erte, I., Forgetta, V., Yang, T.-P., et al.; Multiple Tissue Human Expression Resource (MuTHER) Consortium (2014). An atlas of genetic influences on human blood metabolites. Nat. Genet. *46*, 543–550.

Sivan, A., Corrales, L., Hubert, N., Williams, J.B., Aquino-Michaels, K., Earley, Z.M., Benyamin, F.W., Lei, Y.M., Jabri, B., Alegre, M.L., et al. (2015). Commensal Bifidobacterium promotes antitumor immunity and facilitates anti-PD-L1 efficacy. Science *350*, 1084–1089.

Srinivasan, B., Baratashvili, M., van der Zwaag, M., Kanon, B., Colombelli, C., Lambrechts, R.A., Schaap, O., Nollen, E.A., Podgoršek, A., Kosec, G., et al. (2015). Extracellular 4′-phosphopantetheine is a source for intracellular coenzyme A synthesis. Nat. Chem. Biol. *11*, 784–792.

St Paul, M., and Ohashi, P.S. (2020). The roles of CD8$^+$ T cell subsets in antitumor immunity. Trends Cell Biol. *30*, 695–704.

St Paul, M., Saibil, S.D., Lien, S.C., Han, S., Sayad, A., Mulder, D.T., Garcia-Batres, C.R., Elford, A.R., Israni-Winger, K., Robert-Tissot, C., et al. (2020). IL6 induces an IL22$^+$ CD8$^+$ T-cell subset with potent antitumor function. Cancer Immunol. Res. *8*, 321–333.

Tannahill, G.M., Curtis, A.M., Adamik, J., Palsson-McDermott, E.M., McGettrick, A.F., Goel, G., Frezza, C., Bernard, N.J., Kelly, B., Foley, N.H., et al. (2013). Succinate is an inflammatory signal that induces IL-1β through HIF-1α. Nature *496*, 238–242.

Vallari, D.S., Jackowski, S., and Rock, C.O. (1987). Regulation of pantothenate kinase by coenzyme A and its thioesters. J. Biol. Chem. *262*, 2468–2471.

van der Windt, G.J.W., Everts, B., Chang, C.-H., Curtis, J.D., Freitas, T.C., Amiel, E., Pearce, E.J., and Pearce, E.L. (2012). Mitochondrial respiratory capacity is a critical regulator of CD8+ T cell memory development. Immunity *36*, 68–78.

van der Windt, G.J.W., Chang, C.-H., and Pearce, E.L. (2016). Measuring bioenergetics in T cells using a Seahorse extracellular flux analyzer. Curr. Protoc. Immunol. *113*, 3.16B.1–3.16B.14.

Veldhoen, M., and Duarte, J.H. (2010). The aryl hydrocarbon receptor: fine-tuning the immune-response. Curr. Opin. Immunol. *22*, 747–752.

Vodnala, S.K., Eil, R., Kishton, R.J., Sukumar, M., Yamamoto, T.N., Ha, N.-H., Lee, P.-H., Shin, M., Patel, S.J., Yu, Z., et al. (2019). T cell stemness and dysfunction in tumors are triggered by a common mechanism. Science *363*, eaau0135.

Waldman, A.D., Fritz, J.M., and Lenardo, M.J. (2020). A guide to cancer immunotherapy: from T cell basic science to clinical practice. Nat. Rev. Immunol. *20*, 651–668.

Wang, C., Yosef, N., Gaublomme, J., Wu, C., Lee, Y., Clish, C.B., Kaminski, J., Xiao, S., Meyer Zu Horste, G., Pawlak, M., et al. (2015). CD5L/AIM regulates lipid biosynthesis and restrains Th17 cell pathogenicity. Cell *163*, 1413–1427.

Yeaman, M.R., Filler, S.G., Chaili, S., Barr, K., Wang, H., Kupferwasser, D., Hennessey, J.P., Jr., Fu, Y., Schmidt, C.S., Edwards, J.E., Jr., et al. (2014). Mechanisms of NDV-3 vaccine efficacy in MRSA skin versus invasive infection. Proc. Natl. Acad. Sci. USA *111*, E5555–E5563.

Zhang, Y., Kurupati, R., Liu, L., Zhou, X.Y., Zhang, G., Hudaihed, A., Filisio, F., Giles-Davis, W., Xu, X., Karakousis, G.C., et al. (2017). Enhancing CD8$^+$ T cell fatty acid catabolism within a metabolically challenging tumor microenvironment increases the efficacy of melanoma immunotherapy. Cancer Cell *32*, 377–391.e9.

STAR★METHODS

KEY RESOURCES TABLE

REAGENT or RESOURCE	SOURCE	IDENTIFIER
Antibodies		
CD4 (clone RM-45)	eBioscience	Cat#48-0042-82; RRID: AB_1272194
CD8 (clone 53-6.7)	eBioscience	Cat#48-0081-82; RRID: AB_1272198
IL-2 (clone JES6-5H4)	eBioscience	Cat#25-7021-82; RRID: AB_1235004
IL-17 (clone eBio17B7)	eBioscience	Cat#17-7177-81; RRID: AB_763580
IL-22 (clone Poly5164)	Biolegend	Cat#516404; RRID: AB_2124255
IL-22 (clone IL22JOP)	eBioscience	Cat#17-7222-82; RRID: AB_10597583
IFN-γ (clone XMG1.2)	eBioscience	Cat#45-7311-82; RRID: AB_1107020
TNF-α (clone MP6-XT22)	eBioscience	Cat#11-7321-82; RRID: AB_465418
CD45.1(clone A20)	eBioscience	Cat#17-0453-82; RRID: AB_469398
CD44 (clone IM7)	eBioscience	Cat#45-0441-82; RRID: AB_925746
CD62L (clone MEL-14)	eBioscience	Cat#47-0621-82; RRID: AB_1603256
Human CD3 (clone OKT3)	eBioscience	Cat#25-0037-42; RRID: AB_2573326
Human CD8 (clone RPA-T8)	eBioscience	Cat#11-0088-42; RRID: AB_10669559
Human IL-17 (clone ebio64DEC17)	eBioscience	Cat#12-7179-42; RRID: AB_1724136
Human IL-22 (clone 22URTI)	eBioscience	Cat#50-7229-42; RRID: AB_10598650
IFN-γ Neutralizing (clone XMG1.2)	Biolegend	Cat#505834; RRID: AB_11150776
Human/Mouse TGF-β Neutralizing (clone 1D11.16.8)	eBioscience	Cat#16-9243-85; RRID: AB_2573124
Human IFN-γ Neutralizing (clone B27)	Biolegend	Cat#506531; RRID: AB_2801091
Actin	Sigma	Cat#A2066; RRID: AB_476693
HIF-1α	Caymen Chem	Cat#10006421; RRID: AB_409037
IL-22 Neutralizing (clone IL22JOP)	eBioscience	Cat#16-7222-82; RRID: AB_2016695
CD3 Functional Grade (clone 145-2C11)	eBioscience	Cat#16-0031-82; RRID: AB_468847
CD28 Functional Grade (clone 37.51)	eBioscience	Cat#16-0281-82; RRID: AB_468921
Human CD3 Functional Grade (clone OKT3)	eBioscience	Cat#16-0037-81; RRID: AB_468854
Human CD28 Functional Grade (clone CD28.2)	eBioscience	Cat#16-0289-81; RRID: AB_468926
Human IL-4 Neutralizing (clone 8D4-8)	Biolegend	Discontinued
PDL1 Blocking (clone 10F.9G2)	BioXcell	Cat#BE0101; RRID: AB_10949073
Chemicals, peptides, and recombinant proteins		
Coenzyme A Trilithium Salt	EMD Millipore	Cat#234101
Oligomycin	Sigma	Cat#75351
Etomoxir	Sigma	Cat#E1905
Diethyl Succinate	Sigma	Cat#W237701
Calcium-D Pantothenate	Sigma	Cat#P5155
N-Acetyl-L-cysteine	Sigma	Cat#A9165
ATP	Invitrogen	Cat#R0441
HIF-Inhibitor	EMD Millipore	Cat#400083
CH-223191	EMD Millipore	Cat#182705
Cell Stimulation Cocktail	eBioscience	Cat#00-4970-03
Brefeldin A	eBioscience	Cat#00-4506-51
IL-12	Biolegend	Cat#577002
IL-6	Biolegend	Cat#575702

(*Continued on next page*)

Continued

REAGENT or RESOURCE	SOURCE	IDENTIFIER
TGF-β1	Biolegend	Cat#763102
IL-23	Biolegend	Cat#589002
TNF-α	Biolegend	Cat#575202
6-Formylindolo(3,2-b)carbazole (FICZ)	Enzo Life Science	Cat#BML-GR206-0100
Human IL-6	Biolegend	Cat#570802
Human IL-21	Biolegend	Cat#571202
Human IL-23	Biolegend	Cat#574102
Human TNF-α	Biolegend	Cat#570102
Fixable Viability Dye	eBioscience	Cat#65-0866-14
Mito Tracker Deep Red	Invitrogen	Cat#M22426
Mito Tracker Red CMX Ros	Invitrogen	Cat#M7512
MitoSOX Red	Invitrogen	Cat#M36008
2-NBDG	Invitrogen	Cat#N13195
BODIPY Fl C16	Invitrogen	Cat#D3821
Critical commercial assays		
ATP Quantification Kit	Sigma	Cat#MAK190-1KT
Acetyl Coenzyme A Assay Kit	Sigma	Cat#MAK039
Deposited data		
RNA Sequencing Data	This paper	GEO: GSE187456
Experimental models: Cell lines		
MC-38	Kerafast	Cat#ENH204-FP
B16-Gp33	gift from Dr. Rolf Zinkernagel	N/A
Experimental models: Organisms/strains		
Mouse: WT: C57BL/6	The Jackson Laboratory	Stock#000664
Mouse: HIF Transgenic: B6.129S6(C)-*Gt(ROSA)26Sor*$^{tm3(HIF1A^*)Kael}$/J	The Jackson Laboratory	Stock#009673
Mouse: AhR Flx: Ahr$^{tm3.1Bra}$/J	The Jackson Laboratory	Stock#006203
Mouse: CD4 Cre: B6.Cg-Tg(Cd4-cre) 1Cwi/BfluJ	The Jackson Laboratory	Stock#022071
Mouse: HIF1A Flx: B6.129-*Hif1a*^{tm3Rsjo}/J	The Jackson Laboratory	Stock#007561
Mouse: Vav Cre: B6.Cg-*Commd10*$^{Tg(Vav1-icre)A2Kio}$/J	The Jackson Laboratory	Stock#008610
Mouse: CD45.1: *Ptprc*^{a} *Pepc*^{b}/BoyJ	The Jackson Laboratory	Stock#002014
Mouse: IL22 Cre: C57BL/6-*Il22*$^{tm1.1(icre)Stck}$/J	The Jackson Laboratory	Stock#027524
Mouse: eYFP: B6.129X1-*Gt(ROSA) 26Sor*$^{tm1(EYFP)Cos}$/J	The Jackson Laboratory	Stock#006148
Mouse: P14	Ohashi lab	Pircher et al., 1989
Mouse: SMARTA	Ohashi lab	Oxenius et al., 1998
Mouse: RIP-GP SV40	Ohashi lab	Nguyen et al., 2002
Software and algorithms		
FlowJo V 10.7	FlowJo	https://www.flowjo.com/
Prism 9	GraphPad Software	https://www.graphpad.com/scientific-software/prism/
Agilent Wave Desktop	Agilent	https://www.agilent.com/en/products/cell-analysis/software-download-for-wave-desktop

RESOURCE AVAILABILITY

Lead contact

Further information and requests for resources and reagents should be directed to and will be fulfilled by the lead contact, Pamela S. Ohashi (pohashi@uhnresearch.ca).

Materials availability

This study did not generate new unique reagents.

Data and code availability

- RNA sequencing data has been deposited at GEO and are publicly available as of the date of publication.
- This paper does not report original code.
- Any additional information required to reanalyze the data reported in this paper is available from the lead contact upon request.

EXPERIMENTAL MODEL AND SUBJECT DETAILS

Animals

C57BL/6 were purchased from The Jackson Laboratory and Taconic. LSL-HIF-1a-dPA mice (JAX stock 009673) were obtained from The Jackson Laboratory and bred to Vav-Cre (JAX stock 008610) mice to generate HIF-1α-Transgenic mice. The HIF-1α in these mice has a proline to alanine substitution rendering HIF-1α resistant to degradation by von Hippel Lindau only in cells that express Cre recombinase (Kim et al., 2006). AhR Flx/Flx (JAX stock 006203) crossed to CD4 cre (JAX stock 022071) were both obtained from the Jackson Laboratory and are referred to as AhR $^{-/-}$ mice in the text. HIF-1α Flx/Flx (Jax stock 007561) were crossed to Vav-cre mice and are referred to as HIF $^{-/-}$ in the text. CD45.1 mice were obtained from the Jackson Laboratory (JAX stock 002014). IL-22 cre mice (JAX stock 027524) were crossed to EYFP mice (JAX stock 006148) for fate reporter experiments. Homozygous IL-22 cre mice were used as IL-22 knockout mice (Ahlfors et al., 2014). Generation of P14 mice, which express a transgenic TCR specific for the H2-D^b gp33 peptide of the lymphocytic choriomeningitis virus (LCMV) was described previously (Pircher et al., 1989). SMARTA mice have been described previously (Oxenius et al., 1998). Mice bearing spontaneous pancreatic tumors (RIP-Gp Sv40 mice) have been previously described (Nguyen et al., 2002). Both female and male mice were used for experiments. All mice were maintained at the Ontario Cancer Institute animal facility according to institutional guidelines and with approval of the Ontario Cancer Institute Animal Ethics Committee. Mice were housed with a maximum of 5 mice per cage in a specific pathogen-free facility with access to food and water *ad libitum*.

Human subjects

Written informed consent was obtained from each donor/patient in the studies. Samples were collected and analyzed under Institutional Review Board approved protocols.

Cell lines

B16-gp33 melanoma was a gift from Dr. Rolf Zinkernagel, University of Zurich. MC-38 cell line was purchased from Kerafast. Cells were cultured in a humidified 37C incubator with 5% CO_2. Cell lines were not authenticated.

METHOD DETAILS

Tc Subset polarization

P14 CD8$^+$ T cells were magnetically purified (Miltenyi Biotec) and co-cultured with mature bone marrow dendritic cells (BMDCs) pulsed with gp33 peptide from LCMV (KAVYNFATM) (Dissanayake et al., 2011b) for three days in IMDM (GIBCO) supplemented with 10% FCS, L-glutamine, β-mercaptoethanol, penicillin and streptomycin. For CD4$^+$ T cells, SMARTA CD4$^+$ cells were co-cultured for three to four days with BMDCs pulsed with gp61 from LCMV (GLNGPDIYKGVYQFKSVEFD). Cells were isolated from both male and female mice. To generate Tc or Th subsets, polarizing cocktails were added at the start of the co-culture as follows –Tc1: IL-12 (5 ng/mL), Tc17: IL-6 (20 ng/mL) + TGF-β1 (3 ng/mL) + IL-23 (10 ng/mL) + α-IFN- γ (XMG1.2 - 10 μg/mL), and Tc22: IL-6 (20 ng/mL) + TNF-α (40 ng/mL) + 6-Formylindolo(3,2-b)carbazole (FICZ at 2 ng/mL) + α-IFN- γ (10 μg/mL) + α-TGF-β (1D11.16.8 - 10 μg/mL). For some experiments, naive T cells were activated with anti-CD3 (145-2C11 - 5 μg/mL) and anti-CD28 (37.51 - 1 μg/mL) or previously activated T cells were re-stimulated with anti-CD3 (1 μg/mL) as indicated in the figure legends. All cells were cultured at 37C with 5% CO_2. Cytokines and neutralizing antibodies were purchased from Biolegend and eBioscience. FICZ was purchased from Enzo Life Sciences.

Flow cytometry and antibodies

Antibodies used for flow cytometry were purchased from eBioscience, Biolegend and BD PharMingen. Antibody clones used were: CD4 (RM-45), CD8 (53-6.7), IL-22 (IL22JOP and Poly5164), IL-17 (eBio17B7), IFN-γ (XMG1.2), IL-2 (JES6-5H4), TNF-α (MP6-XT22),

and CD45.1 (A20). For human cells antibody clones used were: CD3 (OKT3), CD8 (RPA-T8), IL-22 (22URTI) and IL-17 (ebio64DEC17). Fc block and fixable viability dye were both purchased from eBiosciences. Antibodies used for western blotting were HIF-1α (Cayman Chem −10006421) and Actin (Sigma - A2066). For intracellular cytokine staining, cells were re-stimulated for 5-6 h with Cell-Stimulation Cocktail (eBioscience) in the presence of Brefeldin A (eBioscience), followed by staining using Cytofix/Cytoperm (BD PharMingen). Flow cytometry data was acquired on a FACSCanto II or Fortessa (BD) and analyzed using FlowJo software (Tree Star).

Metabolomic profiling

Metabolomic profiling of the $CD8^+$ Tc subsets were conducted at Metabolon (Durham, NC) as described previously (Shin et al., 2014). Briefly, cell pellets (n = 5 biological replicates per group) were disrupted using a GenoGrinder (675 strokes/minute, 2 min) and subjected to methanol extraction. Extracts were split into four aliquots and processed for analysis by ultra-high-performance liquid chromatography/mass spectrometry (UHPLC/MS) in the positive (two methods), negative or polar ion mode. Metabolites were identified by automated comparison of ion features to a reference library of chemical standards followed by visual inspection for quality control. For statistical analyses and data display, any missing values were assumed to be below the limits of detection; these values were imputed with the compound minimum (minimum value imputation). To determine statistical significance, Welsh's two-factor t test was performed on protein-normalized data in ArrayStudio (Omicsoft) or "R" to compare data between experimental groups; $p < 0.05$ was considered significant. An estimate of the false discovery rate (Q-value) was calculated to take into account the multiple comparisons that normally occur in metabolomic-based studies, with $Q < 0.05$ used as an indication of high confidence in a result. ArrayStudio was also used to generate high level overview display items (PCA, heatmaps). Pathway enrichment scores for Tc22 were calculated relative to control effector $CD8^+$ T cells using the formula: (# of significant metabolites in pathway(k) / total # of detected metabolites in pathway(m)) / (total # of significant metabolites(n) / total # of detected metabolites(N)) (k/m)/(n/N). A p value threshold of $p < 0.01$ was used. Only pathways where a minimum of 3 metabolites were examined were included.

For metabolic profiling of CoA treated cells, cell pellets from 3 mice were washed and snap frozen in 300 μL methanol. For metabolic profiling of human plasma, 20 μL of plasma was added to 80 μL of HPLC grade methanol. For both cell pellet and plasma analysis, samples were vortexed and incubated for 30 min at −80C to precipitate protein, centrifuged at 15000xg to clarify. 10 μL of supernatant was diluted in 990 μl, of buffer containing 95% acetonitrile, 5% 20 mM ammonium carbonate (pH 9.8) and 1.25 μM metabolomics amino acid mix standard (PN MSK-A2-1.2; Cambridge Isotope Laboratories). Quality control samples (QCs) were prepared by pooling 100 μL of each sample. All samples including QCs, where then analyzed by selected reaction monitoring (SRM) using a Waters XBridge Amide 2.1 × 50 mm, 3.5 μm column and a 20 mM ammonium carbonate (pH 9.8) acetonitrile buffer system coupled with a Sciex Qtrap 5500 triple quadrupole linear ion trap tandem mass spectrometer. The data acquisition included 317 transitions. Data were captured using Analyst, version 1.6.2 software (Sciex); peak integration was performed using Skyline, version 4.1 (Pino et al., 2020). An in-house R script was used for data QC analysis and normalization (Version 3.1.2, http://www.r-project.org). Statistical analysis was performed using the MetaboAnalystR package (Chong et al., 2019).

Metabolic assays

Seahorse was performed as previously described (van der Windt et al., 2012). ATP quantification was performed on CoA-treated T cells using a commercial kit (Sigma) according to the recommended protocol. Mitochondrial mass and potential staining were conducted with flow cytometry using MitoTracker Deep Red (Invitrogen) and MitoTracker Red CMXRos (Invitrogen), respectively, according to manufacturer's recommended protocol. ROS staining was conducted with flow cytometry using MitoSOX Red (Invitrogen) according to the recommended protocol. Acetyl CoA was quantified in T cells following lysis with 1% Triton (Sigma) and de-protonation/detergent removal using 10 kDA spin columns (Amicon). Cell extracts were then analyzed using the Acetyl CoA assay kit (Sigma) according to the recommended protocol. Glucose and fatty acid uptake were conducted using fluorescently labeled 2-NBDG and BODIPY FL C16 (both from ThermoFisher) respectively according to the manufacturers recommended protocol.

Stable isotype tracing analysis

For SITA, $CD8^+$ T cells activated for three days in the presence of vehicle or CoA were harvested, washed and incubated for 2.5 h with U-$^{13}C_6$-glucose (Cambridge Isotopes). Cells were then washed and pellet was frozen in methanol. The cells were thawed on ice and lysed by sonication at 4°C using a Diagenode Bioruptor (30 s. on, 30 s off, 5mins). The resulting mixtures were spun down (15mins 13000rpm 4°C) to remove the cellular debris, the resulting supernatants were transferred to clean microfuge tubes and the solvent was removed using a speed-vac at room temperature. The resulting pellets were stored at −70°C until derivitization. The pellets were solubilized in 30 μL of pyridine containing methoxyamine (10mg/mL; Sigma) and each sample was spiked with 1 μL of myristic acid-D_{27} (750ng/mL in pyridine; Cambridge Isotopes). The samples were vortexed, sonicated, transferred to autoinjection vials and incubated at room temperature for 30mins. Subsequent to this, 70μL of N-tert-Butyldimethylsilyl-N-methyltrifluoroacetamide (MTBSTFA; Sigma) was added and the samples were incubated at 70°C for 30mins. GC/MS analysis was performed using an Agilent 5975C GC/MS equipped with a DB-5MS+DG capillary column. 1μL of sample was injected onto the GC column in splitless mode with an inlet temperature of 280°C and the data was collected by electron impact set at 70 eV. Helium was used as the carrier gas with a flow rate of 1.55 mL/min. The quadrupole was set at 150°C and the GC/MS interface at 285°C. The oven program for all metabolite analyses started at 60°C held for 1 min, then increasing at a rate of 10°C/min until 320°C. Bake-out was at 320°C for 10 min and the sample data were acquired in scan mode (1-600 m/z). The data was analyzed using Agilent MSD-Chemstation interfaced to the NIST11 library.

Metabolite identities were further cross-validated to standards (Sigma) run in-house on the same instrument. Mass isotopomer analysis was used to derive the flux data employing in-house algorithms to take into account ^{13}C natural abundances. Integrated ion intensities are reported relative to the myristic acid-D_{27} internal standard.

Pharmacologic compounds

Oligomycin, Etomoxir, Diethyl succinate, Calcium-D Pantothenate and N-Acetyl-L-cysteine (NAC) were purchased from Sigma, ATP was purchased from Invitrogen, and Coenzyme A Trilithium Salt (CoA), HIF-inhibitor (CAS 934593-90-5) and the AhR antagonist CH-223191 were purchased from EMD Millipore. $CD8^+$ T cells were activated in the presence of polarizing cytokines, and Oligomycin (100 nM) was added 24 h later in the media along with the polarizing cytokines for the last 48 h of activation. The compounds Etomoxir (40 μM), Pantothenate (8 mM), Diethyl Succinate (14 mM), HIF-Inhibitor (40 μM), CH-223191 (500 ng/mL), NAC (15 mM), ATP (0.3 mM) were added at the start of activation with or without the presence of polarizing cytokines or CoA as indicated in the figure legends. CoA was added at the start of activation unless otherwise indicated at a concentration of 2.5-3.5 mM depending on the lot.

RNA extraction and sequencing

RNA was extracted from $CD8^+$ T cells activated for three days in the presence of CoA or Vehicle using QIAGEN RNEasy kit. Libraries were prepared using TruSeq Stranded Total RNA kit. Two hundred nanograms from RNA samples were ribosomal RNA depleted using Ribo-zero Gold rRNA beads, following purification the RNA was fragmented. The cleaved RNA fragments were copied into first strand cDNA using reverse transcriptase and random primers. This is followed by second strand cDNA synthesis using RNase H and DNA Polymerase I. A single "A" based were added and adaptor ligated followed by purification and enrichment with PCR to create cDNA libraries. Final cDNA libraries were size validated using Agilent Bioanalyzer and concentration validated by qPCR. All libraries were normalized to 10nM and pooled together. 10pM of pooled libraries were loaded onto Illumina cBot for cluster generation. Clustered flow cell was then sequenced Pair-end 100 cycles V3 using Illumina HighSeq 2000 to achieve ~30 million reads per sample.

RNA sequencing data analysis

The Tophat (2.0.8b) software suite with Bowtie (2.0.5) was used to align reads to the *Mus musculus* mm10 mouse genome (igenome). RNA_seqc (1.1.7) was used to assess the quality of the aligned data and depletion based on median coverage across transcript length and identities of top expressed transcripts. Samtools (0.1.18) was used to merge aligned technical replicates and sort alignment files. The cufflinks (2.2.1) software suite was used to quantify alignments. Cuffquant was used to quantify individual sample alignments and Cuffnorm was used to normalize quantified data for each group of biological replicates. Cuffdiff was used in conjunction with the R (3.2.2) library CummeRbund (2.10.0) to explore the data at replicate and grouping levels. The RNA sequencing analysis performed for the figures comparing Tc1, Tc17 and Tc22 subsets was derived from a previously published study (St Paul et al., 2020).

Tumor experiments

For B16 melanoma experiments, 8-12 week old female C57BL/6 mice were randomized into different cohorts and inoculated subcutaneously with $4x10^5$ B16F10-gp33 cells and received $0.5x10^6$ activated $CD8^+$ P14 T cells as indicated by tail vein infusion. Tumor size was continually assessed using calipers until mice reached experimental endpoint (diameter $\geq$ 1.5 cm or severe ulceration/necrosis). In some experiments mice also received i.p. administration of 100 μg anti-IL-22 neutralizing antibody (clone – IL22JOP) or isotype control (both purchased from eBiosciences) on the same day and 4 days after the administration of T cells. This dosage of anti-IL-22 has previously been shown to be effective at neutralizing IL-22 in an IL-22 dependent mouse infection model (Yeaman et al., 2014). For pancreatic tumor experiments, RIP-Gp SV40 mice bearing well-established pancreatic tumors (7 days after blood glucose first measures < 5mM) were treated with 1.5×10^6 activated $CD8^+$ P14 T cells. Tumor burden was continuously assessed by measuring blood glucose. In some instances, congenically labeled $CD45.1^+$ P14 T cells were transferred to allow for tracking of transferred cell populations. These mice were sacrificed 18 days post transfer and flow cytometry was performed to analyze expression of $CD8^+$ $CD45.1^+$ T cells in the tumor draining lymph node. For α-PDL1 experiments, 8-12 week old B6 mice were inoculated subcutaneously with $4x10^5$ MC-38 cells. 7 days later, mice with established tumors were randomly allocated to different treatment groups, some of which received an i.p. injection of α-PDL1 (100 μg of clone 10F.9G2 from BioXcell) on day 7 and day 10 post tumor injection. Some mice also received 5 mg of pantothenate i.p. or vehicle control daily starting on day 7 until day 11 post-tumor inoculation.

Human T cell experiments

Peripheral blood mononuclear cells were obtained from healthy donors following institutional review board approval. Written informed consent was obtained from all donors who provided the samples. PBMCs were magnetically sorted for naive T cells (Miltenyi Biotec) and seeded into a 96-well plate previously coated with 5 μg/mL anti-CD3 (eBioscience, clone OKT3). To induce Tc22 polarization, the following antibodies and cytokines were added to culture: 1 μg/mL anti-CD28 (eBioscience, clone CD28.2), 5 μg/mL anti-IFN-γ (BioLegend, clone B27), 5 μg/mL anti-IL-4 (BioLegend, clone 8D4-8), 5 μg/mL anti-TGF-β (eBioscience, clone 1D11.16.8), 20 ng/mL IL-6, 10 ng/mL IL-21, 10 ng/mL IL-23, 40 ng/mL TNF-α (All from BioLegend) and 2 ng/mL FICZ. Pantothenate (8 mM) or vehicle control was also added on day 0. Five days later, cells were stimulated with PMA/ionomycin + Brefeldin for 5-6 h. Cells were then stained and analyzed for intracellular cytokines by flow cytometry.

Human patient cohort

Plasma was collected from patients with stage III or stage IV melanoma prior to the start of receiving anti-PD1 antibody therapy (average 27 days prior). The cohort of patients used is comprised of 21 responders and 21 non-responders. Clinical response (responders) was defined by radiographic evidence of freedom from disease, stable disease, or decreased tumor volume for more than 6 months. Lack of a clinical response (non-responders) was defined by tumor growth on serial CT scans or a clinical benefit lasting 6 months or less. Time to next treatment curve was calculated as interval of days from start of anti-PD1 therapy until start of next treatment or death. Samples were collected and analyzed under Institutional Review Board-approved protocols. These studies were conducted in accordance with the Declaration of Helsinki and approved by the UT MD Anderson Cancer Center IRB. The age and sex of patients can be found in Table S2.

QUANTIFICATION AND STATISTICAL ANALYSIS

Statistical significance was calculated using GraphPad Prism as indicated in the figure legends. $p < 0.05$ was considered statistically significant. * $p < 0.05$, ** $p < 0.01$, ***$p < 0.001$.